

Species-specific activity of antibacterial drug combinations

Ana Rita Brochado¹, Anja Telzerow¹, Jacob Bobonis¹, Manuel Banzhaf^{1,11}, André Mateus¹, Joel Selkirk¹, Emily Huth², Stefan Bassler¹, Jordi Zamarreño Beas³, Matylda Zietek¹, Natalie Ng⁴, Sunniva Foerster⁵, Benjamin Ezraty³, Béatrice Py³, Frédéric Barras^{3,6}, Mikhail M. Savitski¹, Peer Bork^{7,8,9,10}, Stephan Göttig² & Athanasios Typas^{1,7*}

The spread of antimicrobial resistance has become a serious public health concern, making once-treatable diseases deadly again and undermining the achievements of modern medicine^{1,2}. Drug combinations can help to fight multi-drug-resistant bacterial infections, yet they are largely unexplored and rarely used in clinics. Here we profile almost 3,000 dose-resolved combinations of antibiotics, human-targeted drugs and food additives in six strains from three Gram-negative pathogens—*Escherichia coli*, *Salmonella enterica* serovar Typhimurium and *Pseudomonas aeruginosa*—to identify general principles for antibacterial drug combinations and understand their potential. Despite the phylogenetic relatedness of the three species, more than 70% of the drug–drug interactions that we detected are species-specific and 20% display strain specificity, revealing a large potential for narrow-spectrum therapies. Overall, antagonisms are more common than synergies and occur almost exclusively between drugs that target different cellular processes, whereas synergies are more conserved and are enriched in drugs that target the same process. We provide mechanistic insights into this dichotomy and further dissect the interactions of the food additive vanillin. Finally, we demonstrate that several synergies are effective against multi-drug-resistant clinical isolates *in vitro* and during infections of the larvae of the greater wax moth *Galleria mellonella*, with one reverting resistance to the last-resort antibiotic colistin.

To study the characteristics and conservation of drug–drug interactions in bacteria, we selected three gamma-proteobacterial species, *E. coli*, *S. Typhimurium* and *P. aeruginosa*, all of which belong to the highest-risk group for antibiotic resistance³. We used model laboratory strains rather than multi-drug-resistant (MDR) isolates to derive general principles behind drug–drug interactions without being confounded by horizontally transferred antibiotic resistance elements, and to facilitate follow-up experiments and comparisons with previous and future results. To further assess whether drug responses vary between strains of the same species, we included two strains per species (Extended Data Fig. 1a), probing each in up to 79 compounds alone and in pairwise combinations. The compounds comprised 59% antibiotics (covering all major classes), 23% human-targeted drugs and food additives—most of which have reported antibacterial and/or adjuvant activity^{4,5}—and 18% other compounds with known bacterial targets or genotoxic effects, such as proton motive force inhibitors or oxidative damage agents, owing to their potential relevance for antibiotic activity and/or uptake^{6,7} (Extended Data Fig. 1a, Supplementary Table 1). We profiled up to 2,883 pairwise drug combinations in each of the 6 strains (17,050 combinations in total). We assessed each drug combination in a 4×4 tailored-dose matrix (Methods, Supplementary Table 1), used optical density as growth readout and calculated fitness as the growth ratio between drug-treated and untreated cells (Extended Data Figs. 1, 2,

Methods). All experiments were done at least twice, and on average four times, with high replicate correlation (average Pearson correlation = 0.93, Extended Data Fig. 3a, b).

We quantified all drug–drug interactions using the Bliss independence model (Extended Data Fig. 1b, Methods). Consistent with its null hypothesis, interaction scores were zero-centred for all species (Extended Data Fig. 3c). From all the scores (ε) obtained per combination (4×4 dose matrix), we derived a single interaction score ($\bar{\varepsilon}$) that ranged from -1 to 1 (Methods). Synergies and antagonisms were considered significant if $P < 0.05$ (Benjamini–Hochberg corrected, 10,000 repetitions of a two-sided Wilcoxon rank-sum test). Strong interactions had an additional effect size requirement for $|\bar{\varepsilon}| > 0.1$, whereas weak interactions could satisfy the effect-size threshold for one of the two strains of the same species but be slightly below the threshold for the other ($|\bar{\varepsilon}| > 0.06$, Methods). In total, we detected 19% interactions (synergies and antagonisms combined) for *E. coli*, 16% for *S. Typhimurium* and 11% for *P. aeruginosa* (Supplementary Table 2). These hit rates are between the $>70\%$ hit rate for 21 antibiotics previously tested in *E. coli*⁸ and the $<2\%$ hit rate for a larger set of combinations previously tested in a number of different fungal species⁹. Discrepancies are likely due to: (i) drug selection biases, (ii) single-drug concentrations used in previous studies, which increase false-negative and -positive rates, and (iii) different strategies of data analysis. For example, we observed that drugs that lack antibacterial activity engage in fewer interactions (Extended Data Fig. 3e): the previous study in fungi⁹ screened pairwise combinations of 6 antifungals with 3,600 drugs, most of which had no antifungal activity—probably explaining the low number of interactions detected—and the study in *E. coli*⁸ profiled only bioactive antibiotics. Out of the 79 drugs tested here, all had at least 1 interaction, and a median of 5–13 interactions, in the different strains (Extended Data Fig. 3f).

Because, to our knowledge, drug combinations have not previously been systematically probed in bacteria, we lacked a ground truth for benchmarking our dataset. To overcome this limitation, we selected 242 combinations and created a validation set using higher-precision 8×8 checkerboard assays (Extended Data Fig. 4a, b, Supplementary Table 3, Methods). We used this validation set both to assess the performance of our interaction identification approach and to benchmark our screen (Extended Data Fig. 4c, d). Overall, we had a precision and recall of 91% and 74%, respectively. The slightly lower recall can be partially explained by the larger coverage of drug concentration range in the validation experiments, which improves our ability to detect interactions (Extended Data Fig. 5). We confirmed 90% of all the weak interactions that we probed in the validation set ($n = 46$, Extended Data Fig. 6, Supplementary Table 3), which supports the rationale of our interaction identification approach. Indeed, including weak interactions in our

¹European Molecular Biology Laboratory, Genome Biology Unit, Heidelberg, Germany. ²Institute of Medical Microbiology and Infection Control, Hospital of Goethe University, Frankfurt am Main, Germany. ³Laboratoire de Chimie Bactérienne, Institut de Microbiologie de la Méditerranée, CNRS UMR 7283, Aix-Marseille Université, Marseille, France. ⁴Department of Bioengineering, Stanford University, Stanford, CA, USA. ⁵Institute of Social & Preventive Medicine, Institute of Infectious Diseases, University of Bern, Bern, Switzerland. ⁶Institut Pasteur, Paris, France. ⁷European Molecular Biology Laboratory, Structural & Computational Biology Unit, Heidelberg, Germany. ⁸Max-Delbrück-Centre for Molecular Medicine, Berlin, Germany. ⁹Molecular Medicine Partnership Unit, Heidelberg, Germany. ¹⁰Department of Bioinformatics, Biocenter, University of Würzburg, Würzburg, Germany. ¹¹Present address: Institute of Microbiology & Infection, School of Biosciences, University of Birmingham, Birmingham, UK. *e-mail: typas@embl.de

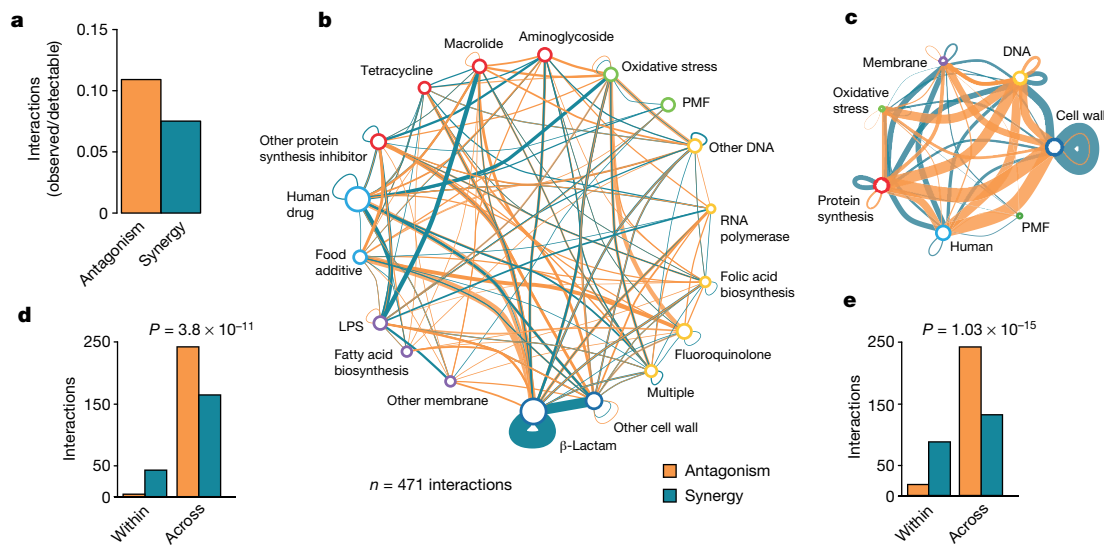


Fig. 1 | Principles of drug–drug interaction networks. **a**, Antagonism is more prevalent than synergy. Fraction of observed over detectable interactions for the six strains. We detect more antagonistic (1,354) than synergistic (1,230) interactions, although our ability to detect antagonisms is lower than our ability to detect synergies (12,778 versus 16,920 combinations). **b, c**, Drug–drug interaction networks in *E. coli*. Nodes represent either drug categories (**b**) or drugs grouped according to the general cellular process that they target (**c**). Node colours represent general cellular processes: blue, cell wall; yellow, DNA; red, protein synthesis; teal, human-targeted or food additive; lilac, membrane; green, oxidative stress or protein motor force (PMF). Node size reflects the number of drugs

hits increases the recall (Extended Data Fig. 4d). For a handful of the synergies observed between antibiotics of the same class (β -lactams), we confirmed the interactions using the Loewe additivity model (Extended Data Fig. 4e), which is more suitable for assessing interactions between drugs with the same target.

Overall, we detected 1,354 antagonistic and 1,230 synergistic interactions. Although this suggests that the two occur with similar frequencies, antagonisms are nearly 50% more prevalent than synergies after correcting for our ability to detect both types of interactions (Fig. 1a). This is because we can detect antagonisms only for 75% of combinations (when at least one drug inhibits growth; Extended Data Fig. 3d, Methods), whereas synergies are detectable for nearly all combinations. A higher prevalence of antagonisms has also been reported for antifungals¹⁰.

Notably, antagonisms and synergies exhibited a clear dichotomy in our data. Antagonism occurred almost exclusively between drugs that target different cellular processes, whereas synergies were also abundant for drugs of the same class or that target the same process (Fig. 1b–e, Extended Data Fig. 7). Mechanistically, antagonism can be explained by interactions at the drug-target level, as the two inhibitors can help the cell to buffer the distinct processes that are perturbed. DNA and protein synthesis inhibitors act this way in bacteria¹¹ (Fig. 1b). Consistent with this being a broader phenomenon, in genome-wide genetic interactions studies in yeast, alleviating interactions (antagonisms) are enriched between essential genes (the targets of anti-infectives), which are part of different functional processes¹². However, antagonism can also occur at the level of intracellular drug concentrations (Extended Data Fig. 8a). We tested 16 antagonistic interactions of different drugs with gentamicin or ciprofloxacin in *E. coli* to investigate the extent to which this occurs. Although initially detected at a growth inhibition level, all antagonisms held true at a killing level, with 14 of the 16 antagonisms working (at least partially) via decreasing the intracellular gentamicin or ciprofloxacin concentrations (Extended Data Fig. 8b). In several of the cases that we tested, this probably occurred because the second drug decreased the proton motive force-energized uptake of gentamicin or increased the AcrAB-TolC-dependent efflux of ciprofloxacin, as antagonisms were neutralized in the respective mutant backgrounds

within category. Edges represent synergy (blue) or antagonism (orange), and thickness reflects the number of interactions. Interactions between drugs of the same category or general cellular target are represented by self-interacting edges. Conserved interactions, including weak interactions, are shown. LPS, lipopolysaccharide. **d, e**, Count of synergistic and antagonistic drug–drug interactions in *E. coli*. Antagonisms occur almost exclusively between drugs that belong to different categories (**d**, across) or target different cellular processes (**e**, across), whereas synergies are also abundant between drugs within the same category (**d**) or that target the same process (**e**). χ^2 -test *P* values are shown for the difference in frequency of synergies over antagonisms between the ‘within’ and ‘across’ groups.

(Extended Data Fig. 8c). Overall, our results suggest that a large fraction of antagonisms is due to modulation of intracellular drug concentrations, rather than to direct interactions of the primary drug targets (Extended Data Fig. 8d, e).

Unlike antagonistic interactions, synergies often occurred between drugs that target the same cellular process (Fig. 1b–e, Extended Data Fig. 7). In fact, synergies are significantly enriched within drugs of the same category across all three species ($P < 10^{-16}$, Fisher’s exact test), given that in our dataset there are about 15-fold-more possible drug combinations across drug categories than within them. Mechanistically, by targeting the same functional process at different steps, drug combinations could bypass the redundancies of this process and thus have a synergistic effect. For example, the many synergies that exist between different β -lactams are probably because of their different affinities to the numerous and often-redundant penicillin-binding proteins (Fig. 1b, Extended Data Figs. 4e, 7a, b).

As with antagonisms, synergies can also occur owing to modulation of intracellular drug concentrations. Consistent with a general permeabilization role of membrane-targeting compounds in many organisms^{9,13,14} and with drug uptake being a major bottleneck for Gram-negative pathogens, one quarter of all the synergies that we detected contained at least one out of the eight membrane-targeting drugs used in our screen (two-sided Wilcoxon rank-sum test, $P = 0.06$). However, membrane-targeting compounds also account for about 18% of antagonisms, which suggests that perturbations in membrane integrity can also decrease intracellular drug concentrations. Consistently, benzalkonium decreases the intracellular concentration of both gentamicin and ciprofloxacin, probably by interfering with their import into the cell (Extended Data Fig. 8b, c).

We next examined the conservation of drug–drug interactions. Interactions within species were highly conserved (Fig. 2a, Extended Data Fig. 9a, b), with conservation being 53–76% depending on the species (Fig. 2b). Conservation is actually higher (68–87%, on average 80%) if we disregard non-comparable interactions for which the concentration range tested precluded us from detecting synergy or antagonism for both strains (Fig. 2b, Extended Data Fig. 3d). The high conservation of

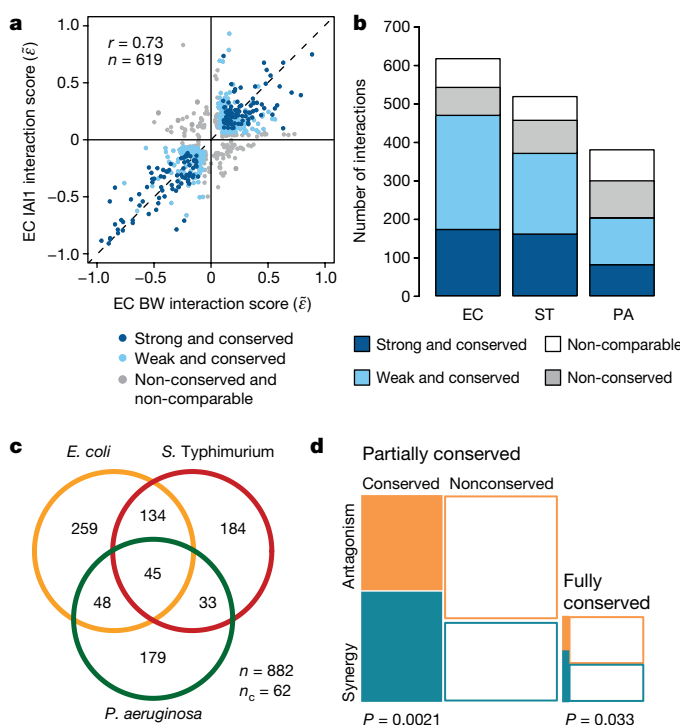


Fig. 2 | Drug–drug interaction conservation. **a**, Drug–drug interactions are conserved in *E. coli*. Scatter plot of interaction scores from the two *E. coli* strains; strong interactions for at least one of the strains are shown. Dark blue, strong and conserved interactions in both strains; light blue, strong interactions in one strain and concordant behaviour in other (weak and conserved); grey, interactions occurring exclusively in one strain or conflicting between strains (non-conserved or non-comparable, which refers to combinations that have considerably different single-drug dose responses between strains (Methods)). r denotes the Pearson correlation, n denotes the number of interactions plotted. **b**, Drug–drug interactions are highly conserved within species. Colours as in **a**; but non-conserved and non-comparable are separated. **c**, Drug–drug interactions are largely species-specific; n = total number of interactions; n_c = conflicting interactions between species, not accounted for in the Venn diagram. **d**, Synergies are more conserved than antagonisms. Mosaic plots and χ^2 -test P values correspond to the quantification of synergy and antagonism among conserved (fully and partially) and non-conserved interactions between species. EC, *E. coli*; EC BW, *E. coli* strain K-12 BW25113; EC IAI1, *E. coli* strain O8 IAI1; ST, *S. Typhimurium*; PA, *P. aeruginosa*.

drug–drug interactions within species is consistent with the finding that these interactions are generally robust to simple genetic perturbations¹⁵. Despite the high degree of conservation within species, 13–32% of the interactions remained strain-specific, with the majority being neutral in the second strain. Very few drug combinations synergized for one strain and antagonized for the other (16 interactions), but such strain differences held in our validation set (Supplementary Table 2).

Although conservation is relatively high within species, it is very low across species (Fig. 2c, Extended Data Fig. 9c). The majority (70%) of interactions occurred in only one species and only 5% were conserved in all three species, despite their close phylogenetic relationship. Because conservation is much higher at the single-drug level across the three species—which share resistance or sensitivity to 73% of the drugs (Supplementary Table 1, Methods)—this indicates that drug combinations can impart species specificity to the drug action. Such specificities can be beneficial for creating narrow-spectrum therapies with low collateral damage, by using synergies that are specific to pathogens and antagonisms that are specific to abundant commensals.

Moreover, we found that despite synergies being less prevalent (Fig. 1a), they are significantly more conserved than antagonisms (Fig. 2d). This is presumably because (i) synergies are enriched between drugs of the same category, and interactions within functional processes

are conserved across evolution¹⁶; (ii) membrane-targeting drugs have a general potentiation effect in Gram-negative bacteria; and (iii) antagonisms often depend on drug import or uptake (Extended Data Fig. 8), which are controlled by less-conserved envelope machineries.

Exploring the network of conserved drug–drug interactions across the three species (Extended Data Fig. 9d) exposed several potential Achilles' heels of Gram-negative bacteria, such as the strong synergy of colistin with macrolides¹⁷, and revealed that known antibiotic classes often behave non-uniformly. For example, the well-known synergy between β -lactams and aminoglycosides is confined to the potent aminoglycosides used in our screen (amikacin and tobramycin) and β -lactams (piperacillin, aztreonam and cefotaxime) that specifically target the cell-division-related penicillin-binding proteins, consistent with previous reports¹⁸. To address whether pairwise drug interactions are driven by mode of action (that is, drug classes interacting in a purely synergistic or antagonistic manner with one another)⁸, we calculated a monochromaticity index for all drug category pairs, across all species (Methods). For highly monochromatic category pairs, the monochromaticity index approaches 1 and -1 for antagonism and synergy, respectively. The monochromaticity index is high overall, especially between well-defined antibiotic classes. Yet, a number of these classes—including β -lactams, tetracyclines and macrolides—have mixed antagonisms and synergies with other antibiotic classes (Extended Data Fig. 9e). β -lactams have diverse affinities to their multiple penicillin-binding-protein targets (potentially explaining the mixed interactions with other classes) but the same does not apply to protein synthesis inhibitors, which have unique targets. In this case, non-uniform class behaviour may be due to different chemical properties of the class members, and thus different dependencies on uptake and efflux systems. Aggregating the monochromaticity index per drug category reinforced the view that broader categories exhibit less concordant interactions (Extended Data Fig. 9f). Besides membrane-targeting drugs, human-targeted drugs were the category that exhibited the most synergies, which suggests that many human-targeted drugs may act as adjuvants.

Because antibiotic classes interacted largely in a monochromatic fashion, clustering drugs according to their interactions recapitulated the class groupings (Extended Data Fig. 10). For example, cell-wall inhibitors grouped together, with further subdivisions being reflective of target specificity. However, exceptions—such as the macrolides, which split—were also evident. Azithromycin, the only dibasic macrolide, separates from its class co-members and clusters with two other basic antibiotics, bleomycin and phleomycin. Compared with other macrolides, azithromycin interacts with and crosses the outer membrane of Gram-negative bacteria in a distinct manner^{17,19} and also has different binding kinetics with the peptide exit tunnel of the 50S ribosomal subunit²⁰. For drugs with unknown or less-well-defined targets, clustering hinted at possible modes of action. Among them, we selected the flavouring compound vanillin, which clusters together with the structurally related acetyl-salicylic acid (aspirin). Salicylate and aspirin induce the expression of the major efflux pump in enterobacteria, AcrAB-TolC, by binding and inactivating the transcriptional repressor MarR²¹ (Fig. 3a). Consistent with a similar action, vanillin treatment increased levels of AcrA protein in *E. coli*, owing to marA overexpression (Fig. 3b, c). Higher AcrA levels upon vanillin or aspirin treatment led to higher minimal inhibitory concentrations for chloramphenicol and ciprofloxacin (Fig. 3d, e). As previously reported for salicylate²², vanillin exerts an additional minor effect on drug resistance in a MarR- and MarA-independent manner (Fig. 3c–e), presumably via the MarA homologue Rob.

To test whether detected interactions are relevant for resistant isolates, we selected seven strong and conserved synergies—comprising antibiotics, human-targeted drugs or food additives—and assessed their efficacy against six MDR *E. coli* and *Klebsiella pneumoniae* clinical isolates in total. All strains were recovered from patients with infections, and belong to successfully spread clonal lineages that contain extended spectrum β -lactamase resistance and various highly prevalent carbapenemases^{23,24}. One *K. pneumoniae* strain (929) is also resistant to the last-resort antibiotic, colistin, owing to a chromosomal mutation

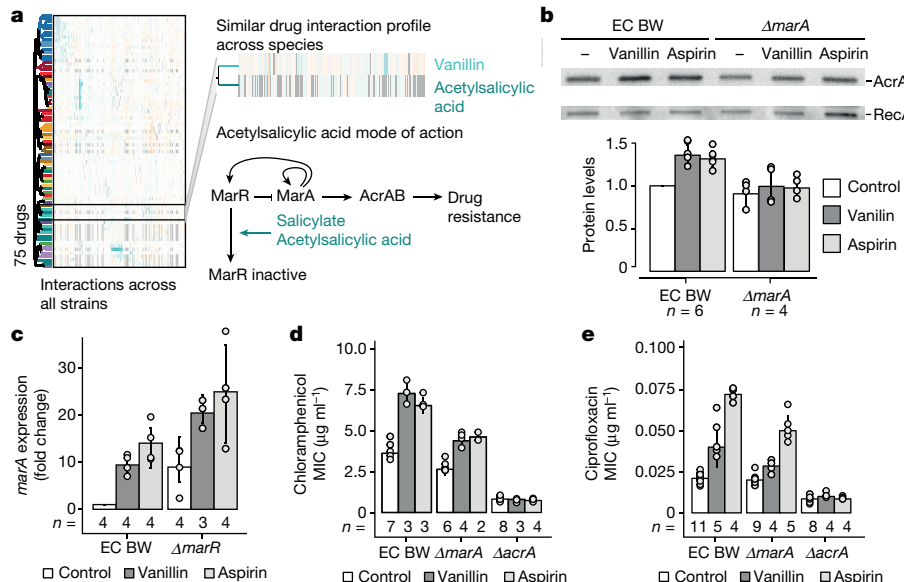


Fig. 3 | Vanillin induces a multi-antibiotic-resistance phenotype.

a, Vanillin and aspirin (acetylsalicylic acid) have similar drug–drug interaction profiles (see Extended Data Fig. 10), which suggests that they have similar modes of action. A schematic of the induction of the multi-antibiotic resistance response through deactivation of the MarR repressor by salicylate or aspirin²¹ is illustrated. b, Vanillin increases AcrA levels in a *marA*-dependent manner. A representative immunoblot of exponentially growing cells (all blots shown in Supplementary Fig. 1) after treatment with solvent, vanillin ($150 \mu\text{g ml}^{-1}$) or aspirin ($500 \mu\text{g ml}^{-1}$) is shown; loading was controlled by cell density and constitutively expressed RecA.

(Supplementary Table 4) that puts the strain in the category of extensively drug-resistant isolates. All drug pairs acted synergistically in most of the strains that we tested (Fig. 4a, Extended Data Fig. 11a). We further tested colistin–clarithromycin and spectinomycin–vanillin with an established infection model for evaluating antibacterial activity, using the larvae of *G. mellonella*. Both combinations also acted synergistically *in vivo* by increasing the rates of *G. mellonella* survival during infection (Fig. 4b, Extended Data Fig. 11b).

The strongest of these synergies is between colistin and different macrolides (Fig. 4, Extended Data Fig. 11). Although other polymyxins are known to help macrolides to cross the outer membrane of Gram-negative bacteria¹⁷, this particular synergy occurred at low colistin concentrations ($<0.3 \mu\text{g ml}^{-1}$) and was active even for the intrinsically colistin-resistant strain (*K. pneumoniae* 929, Fig. 4), which implies that macrolides may also potentiate colistin via an as-yet-unknown mechanism. Similar resensitization of colistin-resistant pathogens to colistin

by macrolides was recently reported for plasmid-borne colistin resistance²⁵, indicating that this synergy is independent of the resistance mechanism. In addition to antibiotic pairs, combinations of human-targeted drugs or food additives with antibiotics were also effective against MDR isolates, even when the former lacked antibacterial activity on their own (Extended Data Fig. 11).

One such compound, vanillin, potentiated the activity of spectinomycin in *E. coli* MDR isolates. This was intriguing, because vanillin antagonizes many other drugs including other aminoglycosides (Supplementary Table 2). We confirmed that this interaction is specific to spectinomycin and vanillin, and not to other aminoglycosides or aspirin, and thus independent of the vanillin effect on AcrAB-TolC (Extended Data Fig. 12a–c). We then probed a genome-wide *E. coli* gene knockout library²⁶ to identify mutations that abrogate the vanillin–spectinomycin interaction, but do not influence the interaction between vanillin and amikacin (another aminoglycoside).

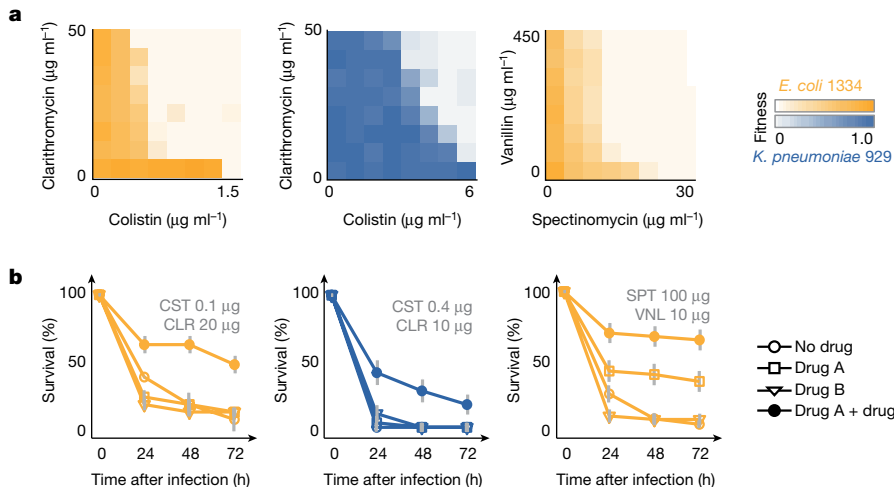


Fig. 4 | Potent synergistic combinations against Gram-negative MDR clinical isolates. a, In vitro synergies, shown as 8×8 checkerboards, for 2 MDR strains (more strains and synergies are shown in Extended Data Fig. 11). One of two biological replicates is shown. b, Drug synergies against the same MDR strains and drug combinations as in a in the *G. mellonella* infection model (see Extended Data Fig. 11). Larvae were infected by *E. coli* and *K. pneumoniae* MDR isolates (10^6 and 10^4 colony-forming units, respectively) and left untreated, treated with single drugs or with a combination of drugs. The percentage of surviving larvae was monitored at indicated intervals after infection. $n = 10$ larvae per treatment. The average of four biological replicates is shown; error bars depict s.d. CST, colistin; CLR, clarithromycin; SPT, spectinomycin; VNL, vanillin.

One of the top hits was *mdfA*, which encodes a transporter of the major facilitator superfamily that exports both charged and neutral compounds²⁷ (Extended Data Fig. 12c). Consistent with MdfA modulating spectinomycin uptake, *ΔmdfA* (*mdfA* deletion mutant) cells were more resistant to spectinomycin and not responsive to vanillin (Extended Data Fig. 12d), whereas cells overexpressing *mdfA* were more sensitive to spectinomycin (Extended Data Fig. 12d, e), as previously reported²⁸, with vanillin further exacerbating this effect (Extended Data Fig. 12d). Vanillin addition also increased the intracellular spectinomycin concentration in an *mdfA*-dependent manner (Extended Data Fig. 12f). At this point, it is unclear how MdfA—which is known to export compounds out of the cell—facilitates spectinomycin import into the cell. However, the phylogenetic occurrence of *mdfA* is concordant with the species-specificity of this interaction, as we detected this synergy in *E. coli* and *S. Typhimurium* but not in *P. aeruginosa* and *K. pneumoniae* isolates, which lack *mdfA*. This synergy underlines the importance of exploring the role of food additives in combinatorial therapies⁵.

In summary, we generated a comprehensive resource of pairwise drug combinations in Gram-negative bacteria, which illuminates key principles of drug–drug interactions and provides a framework for assessing their conservation across organisms or individuals (Supplementary Discussion). Such information can form the basis for similar screens in other microbes, studies investigating the underlying mechanism of pairwise drug combinations^{11,15,29} and computational predictions of their outcomes^{30,31}. Some of the principles that we have identified probably go beyond anti-infectives and microbes³². For antibacterial drug therapies, our study shows that non-antibiotic drugs hold promise as adjuvants, offers a new path for narrow spectrum therapies and identifies effective synergies against MDR clinical isolates (Supplementary Discussion). Further experimentation is required to address whether such synergies have clinical relevance.

Online content

Any Methods, including any statements of data availability and Nature Research reporting summaries, along with any additional references and Source Data files, are available in the online version of the paper at <https://doi.org/10.1038/s41586-018-0278-9>.

Received: 11 May 2017; Accepted: 24 May 2018;

Published online: 04 July 2018

- President of the General Assembly of the United Nations. Press release: high-level meeting on antimicrobial resistance (<http://www.un.org/pga/71/2016/09/21/press-release-hl-meeting-on-antimicrobial-resistance/>) (2016).
- Brown, E. D. & Wright, G. D. Antibacterial drug discovery in the resistance era. *Nature* **529**, 336–343 (2016).
- Tacconelli, E. et al. Discovery, research, and development of new antibiotics: the WHO priority list of antibiotic-resistant bacteria and tuberculosis. *Lancet Infect. Dis.* **18**, 318–327 (2018).
- Ejim, L. et al. Combinations of antibiotics and nonantibiotic drugs enhance antimicrobial efficacy. *Nat. Chem. Biol.* **7**, 348–350 (2011).
- Brown, D. Antibiotic resistance breakers: can repurposed drugs fill the antibiotic discovery void? *Nat. Rev. Drug Discov.* **14**, 821–832 (2015).
- Kohanski, M. A., Dwyer, D. J., Hayete, B., Lawrence, C. A. & Collins, J. J. A common mechanism of cellular death induced by bactericidal antibiotics. *Cell* **130**, 797–810 (2007).
- Erzaty, B. et al. Fe–S cluster biosynthesis controls uptake of aminoglycosides in a ROS-less death pathway. *Science* **340**, 1583–1587 (2013).
- Yeh, P., Tschumi, A. I. & Kishony, R. Functional classification of drugs by properties of their pairwise interactions. *Nat. Genet.* **38**, 489–494 (2006).
- Robbins, N. et al. An antifungal combination matrix identifies a rich pool of adjuvant molecules that enhance drug activity against diverse fungal pathogens. *Cell Reports* **13**, 1481–1492 (2015).
- Cokol, M. et al. Large-scale identification and analysis of suppressive drug interactions. *Chem. Biol.* **21**, 541–551 (2014).
- Bollenbach, T., Quan, S., Chait, R. & Kishony, R. Nonoptimal microbial response to antibiotics underlies suppressive drug interactions. *Cell* **139**, 707–718 (2009).
- Costanzo, M. et al. A global genetic interaction network maps a wiring diagram of cellular function. *Science* **353**, aaf1420 (2016).
- Farha, M. A. & Brown, E. D. Chemical probes of *Escherichia coli* uncovered through chemical–chemical interaction profiling with compounds of known biological activity. *Chem. Biol.* **17**, 852–862 (2010).
- Stokes, J. M. et al. Pentamidine sensitizes Gram-negative pathogens to antibiotics and overcomes acquired colistin resistance. *Nat. Microbiol.* **2**, 17028 (2017).

- Chevereau, G. & Bollenbach, T. Systematic discovery of drug interaction mechanisms. *Mol. Syst. Biol.* **11**, 807 (2015).
- Ryan, C. J. et al. Hierarchical modularity and the evolution of genetic interactomes across species. *Mol. Cell* **46**, 691–704 (2012).
- Vaara, M. Outer membrane permeability barrier to azithromycin, clarithromycin, and roxithromycin in Gram-negative enteric bacteria. *Antimicrob. Agents Chemother.* **37**, 354–356 (1993).
- Giamarelou, H., Zissis, N. P., Tagari, G. & Bouzos, J. In vitro synergistic activities of aminoglycosides and new beta-lactams against multiresistant *Pseudomonas aeruginosa*. *Antimicrob. Agents Chemother.* **25**, 534–536 (1984).
- Imamura, Y. et al. Azithromycin exhibits bactericidal effects on *Pseudomonas aeruginosa* through interaction with the outer membrane. *Antimicrob. Agents Chemother.* **49**, 1377–1380 (2005).
- Petropoulos, A. D. et al. Time-resolved binding of azithromycin to *Escherichia coli* ribosomes. *J. Mol. Biol.* **385**, 1179–1192 (2009).
- Hao, Z. et al. The multiple antibiotic resistance regulator MarR is a copper sensor in *Escherichia coli*. *Nat. Chem. Biol.* **10**, 21–28 (2014).
- Chubiz, L. M., Glekas, G. D. & Rao, C. V. Transcriptional cross talk within the *mar-sox-rob* regulon in *Escherichia coli* is limited to the *rob* and *marRAB* operons. *J. Bacteriol.* **194**, 4867–4875 (2012).
- Göttig, S., Hamprecht, A. G., Christ, S., Kempf, V. A. & Wichelhaus, T. A. Detection of NDM-7 in Germany, a new variant of the New Delhi metallo-β-lactamase with increased carbapenemase activity. *J. Antimicrob. Chemother.* **68**, 1737–1740 (2013).
- Göttig, S., Gruber, T. M., Stecher, B., Wichelhaus, T. A. & Kempf, V. A. In vivo horizontal gene transfer of the carbapenemase OXA-48 during a nosocomial outbreak. *Clin. Infect. Dis.* **60**, 1808–1815 (2015).
- MacNair, C. R. et al. Overcoming *mcr-1* mediated colistin resistance with colistin in combination with other antibiotics. *Nat. Commun.* **9**, 458 (2018).
- Baba, T. et al. Construction of *Escherichia coli* K-12 in-frame, single-gene knockout mutants: the Keio collection. *Mol. Syst. Biol.* **2**, 2006.0008 (2006).
- Yardeni, E. H., Zomot, E. & Bibi, E. The fascinating but mysterious mechanistic aspects of multidrug transport by MdfA from *Escherichia coli*. *Res. Microbiol.* <https://doi.org/10.1016/j.resmic.2017.09.004> (2017).
- Bohn, C. & Bouloc, P. The *Escherichia coli* *cmlA* gene encodes the multidrug efflux pump Cmr/MdfA and is responsible for isopropyl-β-d-thiogalactopyranoside exclusion and spectinomycin sensitivity. *J. Bacteriol.* **180**, 6072–6075 (1998).
- Nichols, R. J. et al. Phenotypic landscape of a bacterial cell. *Cell* **144**, 143–156 (2011).
- Wildenhain, J. et al. Prediction of synergism from chemical–genetic interactions by machine learning. *Cell Syst.* **1**, 383–395 (2015).
- Chandrasekaran, S. et al. Chemogenomics and orthology-based design of antibiotic combination therapies. *Mol. Syst. Biol.* **12**, 872 (2016).
- Lehár, J. et al. Synergistic drug combinations tend to improve therapeutically relevant selectivity. *Nat. Biotechnol.* **27**, 659–666 (2009).

Acknowledgements We thank P. Beltrao (EBI) and T. Bollenbach (University of Cologne) for providing feedback on the manuscript; K. M. Pos (Goethe University) for the anti-AcrA antibody; D. Helm and the EMBL Proteomics Core Facility for help with mass spectrometry experiments; the EMBL GBCS and the Centre for Statistical Analysis for advice on data analysis; S. Riedel-Christ for help with *G. mellonella* experiments; and the members of the Typas laboratory for discussions. This work was partially supported by EMBL internal funding, the Sofja Kovalevskaja Award of the Alexander von Humboldt Foundation to A.Ty., the JPIAMR Combinatorials grant to F.B. (ANR) and A.Ty. (BMBF), and the DFG (FOR 2251) to S.G. A.M. and J.S. are supported by a fellowship from the EMBL Interdisciplinary Postdoc (EIPOD) program under Marie Curie Actions COFUND.

Reviewer information *Nature* thanks A. Koul, K. Lewis and the other anonymous reviewer(s) for their contribution to the peer review of this work.

Author contributions A.R.B. and A.Ty. conceived and designed the study. A.R.B., A.Ty. and J.B. performed the screen; A.R.B., A.Ty. and N.N. the validation screen; and A.R.B., M.B., A.M., J.S., S.B., M.Z. and J.Z.B. the mechanistic follow-up work. S.G. characterized the clinical isolates. A.R.B., A.Ty. and S.F. performed the clinical isolate checkerboards, and E.H. and S.G. performed the *G. mellonella* infection experiments. A.R.B. analysed all data. B.P., F.B., S.G. and A.Ty. supervised different parts of this study; B.E., M.M.S. and P.B. provided advice. A.R.B. and A.Ty. wrote the paper with input from M.M.S., P.B. and S.G. All authors approved the final version.

Competing interests EMBL has filed a patent application on using drug combinations identified in this study for prevention and/or treatment of infections and antibacterial-induced dysfunctions (European patent application number EP18169989.3). A.B., S.G. and A.Ty. are listed as inventors.

Additional information

Extended data is available for this paper at <https://doi.org/10.1038/s41586-018-0278-9>.

Supplementary information is available for this paper at <https://doi.org/10.1038/s41586-018-0278-9>.

Reprints and permissions information is available at <http://www.nature.com/reprints>.

Correspondence and requests for materials should be addressed to A.Ty.

Publisher's note: Springer Nature remains neutral with regard to jurisdictional claims in published maps and institutional affiliations.

METHODS

No statistical methods were used to predetermine sample size.

Strains, plasmids and drugs. For each of the three Gram-negative species profiled in this study, we used two common sequenced laboratory strains: *E. coli* K-12 BW25113 and O8 IAI1 (hereafter IAI1), *S. Typhimurium* LT2 and 14028s, and *P. aeruginosa* PAO1 and PA14. To validate selected synergies, we profiled 6 MDR clinical Enterobacteriaceae isolates recovered from specimens from human patients: *E. coli* 124, 1027 and 1334, and *K. pneumoniae* 718, 929 and 980 (see Supplementary Table 4 for details of antibiotic resistance determinants). For follow-up experiments, we used two closely related *E. coli* K-12 model strains, BW25113 and MG1655.

All mutants used in this study were made using the *E. coli* Keio knockout collection²⁶, after confirming with PCR and retransducing the mutation to wild-type BW25113 with the P1 phage (Supplementary Table 5). The kanamycin resistance cassette was excised when necessary using the plasmid pCP20³³. The plasmid used for *mdfA* overexpression was obtained from the mobile *E. coli* ORF library³⁴.

Drugs used in this study were purchased from Sigma Aldrich, except for metformin hydrochloride (TCI Chemicals), clindamycin and bleomycin (Applichem), CHIR-090 (MedChemtronica) and vanillin (Roth). Stocks were prepared according to the supplier's recommendations (preferably dissolved in water).

Minimal inhibitory concentration calculation. We defined minimal inhibitory concentration (MIC) as the lowest concentration required to inhibit growth of a microorganism after 8 h of incubation in lysogeny broth (LB) at 37 °C with shaking (384-well plates, starting with an optical density at 595 nm (OD_{595 nm}) of 0.01). MICs of all drugs were computed using a logistic fit of growth (OD_{595 nm} for 8 h) over twofold serial dilutions of the antibiotic concentrations for all strains used for the high-throughput screening and follow-up experiments.

High-throughput screening of pairwise drug interactions. For all drug combination experiments, drugs were diluted in LB to the appropriate working concentrations in transparent 384-well plates (Greiner BioOne GmbH), with each well containing 30 µl in total. After the addition of drugs, cells were inoculated at initial OD_{595 nm} of about 0.01 from an overnight culture. The same inoculum was used for all strains. All liquid handling (drug addition and cell mixing) was done with a Biomek FX liquid handler (Beckman Coulter). Plates were sealed with breathable membranes (Breathe-Easy) and incubated at 37 °C in a humidity-saturated incubator (Cytomat 2, Thermo Scientific) with continuous shaking and without lids to avoid condensation. OD_{595 nm} was measured every 40 min for 12 h in a Filtermax F5 multimode plate reader (Molecular Devices).

A flowchart of the experimental and analytical pipeline is shown in Extended Data Fig. 2a. Data analysis was implemented with R and networks were created with Cytoscape³⁵.

Experimental pipeline. The drug–drug interaction screen was performed using 4 × 4 checkerboards. Sixty-two drugs were arrayed in 384-well plates with the different concentrations in duplicates (array drugs). Each plate contained 12 randomly distributed wells without arrayed drug: 9 wells containing only the query drug, and 3 wells without any drug. One query drug at a single concentration was added to all wells of the 384-well plate, except for the 3 control wells. All drugs were queried once—or occasionally twice—per concentration. We used 78 drugs as query in *E. coli* and *S. Typhimurium*, and 76 in *P. aeruginosa*. In total, 79 query drugs were screened, out of which 75 were common to all three species (Supplementary Table 1). The 62 array drugs were a subset of the 79 query drugs. The same drug concentrations were used in both query and array drugs (Supplementary Table 1). Three drug concentrations (twofold dilution series) were selected based on the MIC curves, tailored to the strain and drug. We targeted for nearly full, moderate and mild or no growth inhibition, which on average corresponded to 50–100%, 25–50% and 0–25% of the MIC, respectively. The highest drug concentration and the lowest fitness obtained per single drug are listed in Supplementary Table 1. For drugs that do not inhibit growth on their own, we selected concentrations according to sensitivity of other strains or species, or to their use in clinics or for research. *E. coli* and *S. Typhimurium* exhibited largely similar single-drug dose responses within species, thus the same drug concentrations were used for both strains of each species. For *P. aeruginosa*, MICs often differed by several fold and drug concentrations were therefore adjusted between the two strains (Supplementary Table 1).

Growth curve analysis. The Gompertz model was fitted to all growth curves (when growth was observed) by using the R package grofit version 1.1.1-1 for noise reduction. Quality of fit was assessed by Pearson correlation (*r*), which was >0.95 for approximately 95% of all growth curves. *r* < 0.95 was indicative of either non-sigmoidal-shaped growth curves—typical of some drugs such as fosfomycin—or noisy data. Noisy data were removed from further analysis. Plate effects were corrected by fitting a polynomial to the median growth of each row and column. The background signal from LB was removed by subtracting the median curve of the non-growing wells from the same plate. These were wells in which either the single- or the double-drug treatments fully inhibited growth; each plate contained

at least three such wells. Data were processed per strain and per batch to correct for systematic effects.

Fitness estimation. We used a single time-point OD_{595 nm} measurement (growth) for assessing fitness. This corresponded to the transition to stationary phase for cells grown without perturbation, as this enables us to capture the effect of drugs on lag-phase, growth rate or maximum growth. Thus, we used OD_{595 nm} at 8 h for *E. coli* BW25113 and both *P. aeruginosa* strains, at 7 h for the fast-growing *E. coli* IAI1 and *S. Typhimurium* 14028s, and at 9 h for the slower-growing *S. Typhimurium* LT2.

We used the Bliss model to assess interactions as it can accommodate drugs that have no effect alone, but which potentiate the activity of others (adjutants)³⁶. This feature is especially relevant here, because we probed intrinsically antibiotic-resistant microbes (*P. aeruginosa* and MDR clinical isolates), and human-targeted drugs or food additives that lack antibacterial activity. According to the Bliss independence model³⁷ and assuming that drug–drug interactions are rare, for most drug combinations the fitness of arrayed drugs (*f_a*) equals the fitness in the presence of both drugs (*f_{aq}*) divided by the fitness of the query drug alone (*f_q*):

$$\varepsilon = f_{\text{aq}} - f_{\text{a}} \times f_{\text{q}} \quad (1)$$

If $\varepsilon = 0$,

$$f_{\text{a}} = \frac{f_{\text{aq}}}{f_{\text{q}}} \Leftrightarrow f_{\text{a}} = \frac{g_{\text{aq}}/g_0}{g_{\text{q}}/g_0} \Leftrightarrow f_{\text{a}} = \frac{g_{\text{aq}}}{g_{\text{q}}} \quad (2)$$

in which ε denotes the Bliss score, f denotes fitness, g denotes growth, subscript a denotes that the variable pertains to an arrayed drug, subscript q denotes that the variable pertains to a query drug and 0 denotes no drug. The fitness in the presence of both drugs (*f_{aq}*) was calculated by dividing the growth in the presence of both drugs (*g_{aq}*) by the median of the growth of drug-free wells from the same plate (*g₀*). The fitness of the single query drugs (*f_q*) was obtained by dividing the top 5% growing wells across each batch by the median of the growth of drug-free wells of each plate (*g₀*). This metric is more robust to experimental errors than using only the 9 wells containing the query drug alone. Nevertheless, both estimators for *f_q* yield very similar results (Pearson correlation, *r* = 0.98). Consistent with equation (2), the fitness of arrayed drugs (*f_a*) was estimated by the slope of the line of best fit between *g_{aq}* and *g_q* across all plates (query drugs) within a batch.

$$\begin{bmatrix} g_{q_1} \\ \vdots \\ g_{q_n} \end{bmatrix}_{n \times 1} \times f_{a_m} = \begin{bmatrix} g_{a_m q_1} \\ \vdots \\ g_{a_m q_n} \end{bmatrix}_{n \times 1} \quad 1 \leq m \leq nr \text{ (number of arrayed drugs)}$$

for a given array drug *m* (*a_m*) across *n* query drugs (*q_n*) within a batch (Extended Data Fig. 2b).

For array drugs with a Pearson correlation (*r*) between *g_{aq}* and *g_q* below 0.7, *f_a* was estimated using only the query drugs that corresponded to the interquartile range of *g_{aq}/g_q* (minimum *n* = 18 query drugs, Extended Data Fig. 2b). Wells for which *r* was still below 0.7, even after restricting the number of plates were removed from further analysis owing to high noise (~2%). For wells exhibiting no growth for >75% of the plates within a batch, *f_a* was deemed to be zero.

Bliss independence interaction scores. Bliss scores (ε) were calculated for each well, as described in equation (1). At least 3×3 drug concentrations $\times 2$ (duplicates) $\times 2$ (query and array drugs) = 36, or 18 (drugs used only as query) scores were obtained per drug pair. Drug–drug interactions were inferred based on the Bliss independence model in three steps: (i) strong interactions based on complete ε distributions, (ii) strong interactions based on ε distributions restricted to relevant drug concentrations and (iii) weak and conserved interactions within species. Cross-species comparisons, drug–drug interaction networks and monochromaticity analyses shown in this study include all drug–drug interactions.

Strong drug–drug interactions based on complete ε distributions. Strong drug–drug interactions were statistically assigned using a re-sampling approach. Ten thousand repetitions of a two-sided Wilcoxon rank-sum test (per drug pair and per strain) were performed, to sample a representative set of ε for a given strain. For every repetition, the ε distribution of a given combination was compared to an ε distribution of the same size randomly sampled from the complete ε set for a given strain. *P* values were calculated as follows:

$$P = \frac{\sum_{n=1}^N (P_n > 0.1) + 1}{N + 1}$$

in which *N* is the total number of repetitions (10,000) and *P_n* is the *P* value of the Wilcoxon rank-sum test obtained for the *n*th repetition. Strong drug–drug interactions were assigned to drug pairs that simultaneously satisfied two criteria: (i) first or third quartile of the ε distribution below −0.1 or higher than 0.1 for synergies or antagonisms, respectively, and (ii) *P* < 0.05 (after correcting for multiple

testing, Benjamini–Hochberg). Only one-sided drug interactions were taken into account, thus the very few interactions that satisfied the criteria concurrently for synergy and antagonism were re-assigned as neutral (only $n = 1$ for $|\tilde{\varepsilon}| > |0.1|$). The highest absolute ε value between the first and third quartiles was used as single interaction score ($\tilde{\varepsilon}$) to reflect the strength of the drug–drug interactions.

Strong drug–drug interactions based on ε distributions restricted to relevant drug concentrations. Because drug interactions are dependent on concentration, the same statistical procedure was repeated after restricting the drug concentration ratios to those relevant for either synergy or antagonism. This constraint was added by excluding ε values that corresponded to concentration ratios in which the expected fitness (product of the fitness on single drugs, $f_x \times f_y$) was below 0.2 for synergy and above 0.8 for antagonism, which represent blind spots for the given interaction type (Extended Data Fig. 3d). These interactions are described by their P value and $\tilde{\varepsilon}$ obtained with restricted drug concentration ratios. Although most interactions were detected based on both full and restricted ε distributions, each of the different methods uniquely identified interactions (Extended Data Fig. 4c). With the expected fitness cutoff of 0.2, we identified the highest number of strong interactions (1,950) with 90 uniquely identified interactions from full ε distributions and 379 from restricted ε distributions (see also ‘Sensitivity analysis’).

Restricting ε values based on expected fitness also enables defining whether synergy or antagonism is detectable for any given drug pair. No significant P value was found for drug pairs with less than five ε scores within the relevant expected fitness space, as their sample size is insufficient. Synergy and antagonism could not be detected for 1% and 25% of all drug combinations, respectively.

Weak and conserved drug–drug interactions within species. For drug pairs with a strong drug–drug interaction in only one of the two strains per species, the criteria for assigning interactions for the second strain was relaxed to $|\tilde{\varepsilon}_{\text{second strain}}| > 0.06$, provided that the interaction sign was the same. Interactions assigned with this approach are termed weak and conserved.

Loewe additivity interaction scores. For combinations between β -lactams for which high-resolution 8×8 checkerboards with sufficient growth inhibition were available in the validation dataset, Loewe additivity³⁸ was used to confirm the interactions. Drug–drug interactions were inferred by the shape of the isoboles (lines of equal growth) in two-dimensional drug-concentration plots. Unless stated otherwise, all isoboles correspond to 50% growth inhibition (IC_{50}) and were obtained by fitting a logistic model, with lines representing isoboles and dots representing IC_{50} interpolated concentrations. To interpolate IC_{50} concentrations (or other percentages of growth inhibition), a logistic model was used to fit the growth for each concentration of the first drug across different concentrations of the second drug. The null hypothesis of this model is represented by the additivity line: a linear isobole connecting equal individual growth inhibition values for the two drugs.

Sensitivity analysis. We confirmed the adequacy of the main statistical parameters used to assign interactions by performing a sensitivity analysis. Several expected fitness ($f_x \times f_y$) cutoffs were tested, while keeping the other parameters constant (Extended Data Fig. 4c). The added value of restricting the ε distributions to relevant drug concentrations (based on expected fitness) was strongly supported by the proportion of strong drug–drug interactions that was found exclusively using this criterion (~19% with our selected cutoff). The selected cutoff (0.2; disregarding wells with $f_x \times f_y < 0.2$ for synergies and with $f_x \times f_y > 0.8$ for antagonisms) resulted in the largest number of total interactions assigned, and the highest precision (91%) and recall (74%) after benchmarking against the validation dataset (Extended Data Fig. 4c).

The suitability of the thresholds applied to define strong ($|\tilde{\varepsilon}| > 0.1$) and weak ($|\tilde{\varepsilon}| > 0.06$) interactions was assessed by their effect on the true- and false-positive rates (Extended Data Fig. 4d). A threshold of $|\tilde{\varepsilon}| > 0.1$ is beneficial, as it imposes a minimum strength to assign interactions. A value of 0.1 corresponds to ~3 times the median of the first and third quartiles across all ε distributions (Extended Data Fig. 2c). Lowering this threshold results in lower true-positive rate, because several drug pairs are reassigned as neutral owing to ambiguity in calling interactions (we do not allow interactions to be both a synergy and an antagonism). Increasing this threshold lowers the true-positive rate, because only very strong interactions will be assigned (Extended Data Fig. 4d). Drug–drug interactions are highly conserved within species, which is evident from the high correlation for $\tilde{\varepsilon}$ that is observed for all species (Fig. 2a, Extended Data Fig. 9a, b). This motivated us to relax the interaction-strength threshold for the second strain if the interaction score $|\tilde{\varepsilon}|$ was above 0.1 in the first strain, dubbing these interactions weak and conserved. By including weak and conserved interactions in our analysis, the true-positive rate was increased by 15%. Adding a threshold for weak interactions of $|\tilde{\varepsilon}| > 0.06$ (about two times the median of the first and third quartiles of all ε distributions) is key for maintaining a low false-positive rate (Extended Data Fig. 4d).

Benchmarking and clinical isolates checkerboard assays. Eight-by-eight checkerboard assays were performed to validate our screen (242 drug combinations in the benchmarking dataset, Supplementary Table 3), and to test 7 selected synergies against 6 MDR clinical isolates (Fig. 4, Extended Data Fig. 11). As in the screen,

growth was assessed on the basis of $OD_{595\text{ nm}}$ at the transition to stationary phase for the no-drug controls. The time points used in the screen were used again for the validation set, and 8 h was used for all *E. coli* and *K. pneumoniae* MDR isolates. Fitness was calculated by dividing $OD_{595\text{ nm}}$ after single- or double-drug treatment by no-drug treatment for each individual checkerboard. Bliss scores (ε) were calculated as before, resulting in 49 ε values per drug pair. Drug combinations were analysed on the basis of ε distributions, after removing wells in which one of the drugs alone—and its subsequent combinations with the second drug—completely inhibited growth. Antagonism was assigned when the median of the ε distribution was above 0.1, or the third quartile was above 0.15. Similarly, synergies were assigned when the median of the ε distribution was below -0.1 or the first quartile was below -0.15. All experiments were done in biological duplicates, and interactions were considered effective when duplicates were consistent (as was the case for the vast majority of interactions).

Assessing conservation of drug–drug interactions. Conservation of drug–drug interactions between strains of the same species was assessed by Pearson correlation of the interactions scores, $\tilde{\varepsilon}$. For potentially non-conserved drug–drug interactions, the expected fitness distributions of the two strains were taken into account. When the two distributions were significantly different according to a two-sided Wilcoxon rank-sum test ($P < 0.05$ after Benjamini–Hochberg correction for multiple testing), the drug pairs were deemed as non-comparable between the two strains.

To assess the cross-species conservation of drug–drug interactions, we took into account only drug pairs that were probed in all three species. Drug–drug interactions were defined as being detected within a species when detected in at least one of the two strains and when no change of interaction sign was observed for the other strain. Interactions were then compared across the three species. Cases in which an interaction between drugs changed from synergy to antagonism or vice versa across species (conflicting interactions; ~7% of all interactions, Supplementary Table 2) were excluded from the comparative ‘across-species’ Venn diagram (Fig. 2c). In current analysis, a given drug–drug interaction may be conserved across species but not conserved within the species.

Conservation at the single-drug level was defined on the basis of shared resistance and sensitivity (Supplementary Table 1). A strain was considered sensitive to a given drug if one of the drug concentrations resulted in at least 30% growth inhibition. Consistent with conservation of drug–drug interactions across species, single-drug responses are conserved across species when at least one strain of both species has the same sign (sensitive or resistant).

Monochromaticity index. The monochromaticity index (MI) between drug pairs has previously been defined³⁹ as: if $r_{ij} > b$, then

$$MI_{ij} = \frac{(r_{ij} - b)}{1 - b}$$

if $r_{ij} = b$, then $MI_{ij} = 0$
and if $r_{ij} < b$, then

$$MI_{ij} = \frac{(r_{ij} - b)}{b}$$

in which r_{ij} denotes the ratio of antagonism to all interactions between drugs from classes i and j , and b denotes the ratio of antagonism to all interactions. We set a minimum of two interactions between drugs from classes i and j to calculate the monochromaticity index. The monochromaticity index equals 1 if only antagonisms occur between drugs from classes i and j , and -1 if only synergies occur between the classes. The monochromaticity index equals zero if the fraction of antagonism between the two classes reflects the background ratio b . Both strong and weak drug interactions were taken into account across all species, to obtain one monochromaticity index per drug category pair.

Assessment of drug combinations in the *G. mellonella* infection model. Larvae of the greater wax moth (*G. mellonella*) at their final instar larval stage were used as an *in vivo* model to assess efficacy of drug combinations. Larvae were purchased from UK Waxworms and TZ-Terraristik. Stock solutions of vanillin (in 20% DMSO), spectinomycin, colistin and clarithromycin (in 20% DMSO and 0.01% glacial acetic acid) were freshly prepared and diluted in PBS to the required concentration. Drugs and bacterial suspensions were administered by injection of 10- μ l aliquots into the haemocoel through the final pair of prolegs (bacteria into the left proleg, and antibiotics into the right), using Hamilton precision syringes. Controls included both uninfected larvae, and infected and uninfected larvae that were injected with the solvent used for the drugs. Drug toxicity was pre-evaluated by injection of serial dilutions of either single drugs or drug combinations, and drugs were used at amounts that caused little or no toxicity. To identify an optimal inoculum, time-kill curves were generated by inoculating larvae with 10 μ l of serially diluted bacterial suspensions (1×10^2 – 1×10^7 CFUs). For final experiments, groups of ten larvae were injected per strain–drug combination, placed into

Petri dishes and incubated at 37 °C. Larvae were infected with a sublethal dose of 1×10^6 and 1×10^4 CFUs for *E. coli* and *K. pneumoniae* isolates, respectively, and subsequently injected with indicated drugs, 1-h after infection. Survival of the larvae was monitored at the indicated time points by two observers independently. Each strain–drug combination was evaluated in four independent experiments.

Cell viability assays and intracellular antibiotic concentration. *Ciprofloxacin*. Overnight cultures of *E. coli* BW25113 were diluted 1:1,000 into 50 ml LB and grown at 37 °C to OD_{595 nm} ~ 0.5. Paraquat (50 µg/ml), vanillin (150 µg/ml), benzalkonium (5 µg/ml), caffeine (200 µg/ml), doxycycline (0.5 µg/ml), rifampicin (5 µg/ml), trimethoprim (5 µg/ml) or curcumin (100 µg/ml) were added to the cultures and incubated at 37 °C for 30 min. Ciprofloxacin (2.5 µg/ml final concentration) was then added to the cultures and cultures were incubated at 37 °C for 1 h in the presence of both drugs. Cell viability was determined by counting CFUs after plating washed cell pellets onto LB agar Petri dishes and incubating for 16 h. Intracellular ciprofloxacin was quantified using liquid chromatography coupled to tandem mass spectrometry (LC–MS/MS), as previously described^{40,41}. Non-washed cell pellets⁴² were directly frozen and lysed with 350 µl of acetonitrile, followed by three freeze–thaw cycles (thawing was performed in an ultrasonic bath for 5 min). Cell debris was pelleted at 16,000g and the supernatant was filtered through a 0.22-µm syringe filter before injection. Chromatographic separation was performed on a Waters BEH C18 column (2.1 × 50 mm; 1.7 µm) at 40 °C, with a 2-min gradient with flow rate of 0.5 ml/min: (i) 0–0.5 min, 1% mobile phase B; (ii) 0.5–1.2 min, linear gradient from 1 to 95% mobile phase B; (iii) 1.2–1.6 min, 95% mobile phase B; and (iv) 1.6–1.7 min, return to initial conditions. Mobile phase A consisted of 0.1% formic acid in water, and mobile phase B consisted of 0.1% formic acid in acetonitrile. Samples were kept at 4 °C until analysis. Sample injection volume was 5 µl. Detection of ciprofloxacin was performed on a Waters Q-Tof premier instrument with electrospray ionization in positive mode. The transition 332 > 314 was monitored, with cone voltage set at 8 and collision energy set at 20. Intracellular ciprofloxacin was normalized to CFUs at the time of ciprofloxacin addition.

Gentamicin. Intracellular gentamicin was quantified by measuring [³H]-gentamicin (1 mCi/ml; Hartmann Analytic), as previously described⁷. Overnight cultures of *E. coli* MG1655 (the parental strain of BW25113) were diluted 1:100 into 5 ml LB and grown to OD_{595 nm} ~ 0.1. [³H]-Gentamicin was diluted in cold gentamicin to obtain a 5 µg/ml (0.1 mCi/ml) stock solution, which was then added to the culture at a final concentration of 5 µg/ml (0.1 µCi/ml) together with the second drug: berberine (200 µg/ml), erythromycin (15 µg/ml), metformin (13,000 µg/ml), procaine (6,000 µg/ml), loperamide (400 µg/ml), benzalkonium (5 µg/ml), rifampicin (5 µg/ml) or clindamycin (200 µg/ml). Cultures were then incubated at 37 °C on a rotary shaker. At 0, 0.5, 1, 1.5 and 2-h time-points, 500-µl aliquots were removed and applied to a 0.45-µm-pore-size HAWP membrane filter (Millipore) pretreated with 1 ml of unlabelled gentamicin (250 µg/ml). Filters were washed with 10 ml of 1.5% NaCl, placed into counting vials and dried for 30 min at 52 °C. Subsequently, 8 ml of liquid scintillation was then added to the dried filters and vials were incubated overnight at room temperature before being counted for 5 min. Gentamicin uptake efficiency is expressed as total accumulation of gentamicin (in ng) per 10^8 cells. Cell viability was determined by CFUs.

Spectinomycin. Intracellular spectinomycin was quantified by measuring [³H]-spectinomycin (1 µCi/mg; Hartmann Analytic). Overnight cultures of *E. coli* BW25113 were diluted 1:1,000 into 1 ml LB with and without vanillin (150 µg/ml) and grown to OD_{595 nm} ~ 0.5. Then, 50 µg/ml [³H]-spectinomycin:spectinomycin 1:100 was added and the cultures were incubated for 1 h. Cultures were pelleted, washed twice with PBS with 50 µg/ml non-labelled spectinomycin, re-suspended in 1% SDS and incubated for 20 min at 85 °C. The lysate was mixed with 8 ml liquid scintillation (Perkin Elmer ULTIMA Gold) and counted for 1 min using a Perkin Elmer Tri-Carb 2800TR. Measured radioactivity was normalized to cell number as measured by OD_{595 nm}.

RNA isolation, cDNA preparation and quantitative RT–PCR. Overnight cultures of *E. coli* BW25113 and the *marR* deletion mutant ($\Delta marR$) were diluted 1:2,000 into 20 ml LB and grown at 37 °C to OD_{595 nm} ~ 0.2. Aspirin or vanillin were added to the cultures to a final concentration of 500 and 150 µg/ml, respectively (DMSO was added in the control), followed by a 30-min incubation period at 37 °C with agitation. Cells were collected and RNA was extracted using the RNeasy Protect Bacteria Mini Kit (Qiagen). cDNA was prepared for RT–qPCR using SuperScript III Reverse Transcriptase (Thermo Fisher Scientific). Levels of *marA* expression were estimated by RT–qPCR using SYBR Green PCR master mix following the manufacturer's instructions (Thermo Fisher Scientific). Primer sequences for *marA* and *recA* were as previously described²⁹. All experiments were conducted in at least three biological replicates, and relative expression levels were estimated as previously described⁴³, using *recA* expression as reference.

Immunoblot analysis for protein quantification. Overnight cultures of *E. coli* BW25113 and the *marA* deletion mutant ($\Delta marA$) were diluted 1:1,000 into 50 ml LB containing 500 µg/ml aspirin, 150 µg/ml vanillin or DMSO (solvent control), followed by growth with agitation at 37 °C to OD_{595 nm} ~ 0.5. Cells were washed

in PBS containing corresponding drugs or DMSO, then resuspended to match OD_{595 nm} = 1. Cell pellets were resuspended in Laemmli buffer and heated to 95 °C for 3 min followed by immunoblot analysis with anti-AcrA polyclonal antiserum (gift from K. M. Pos) at 1:200,000 dilution. Primary antiserum was detected using anti-rabbit HRP (A0545 Sigma) at 1:5,000 dilution. Cell loading was controlled with the anti-RecA antibody (rabbit, ab63797 Abcam). For densitometry analysis, the pixel intensity of AcrA bands from cell-density-normalized samples was quantified using ImageJ. At least four different biological replicates were blotted. Each biological replicate was run and blotted twice (technical replicates). Relative AcrA levels per biological replicate correspond to the average intensities of the technical replicates. All blots can be found in Supplementary Fig. 1.

Screening the *E. coli* Keio knockout collection for identifying the mode of action of drug interactions.

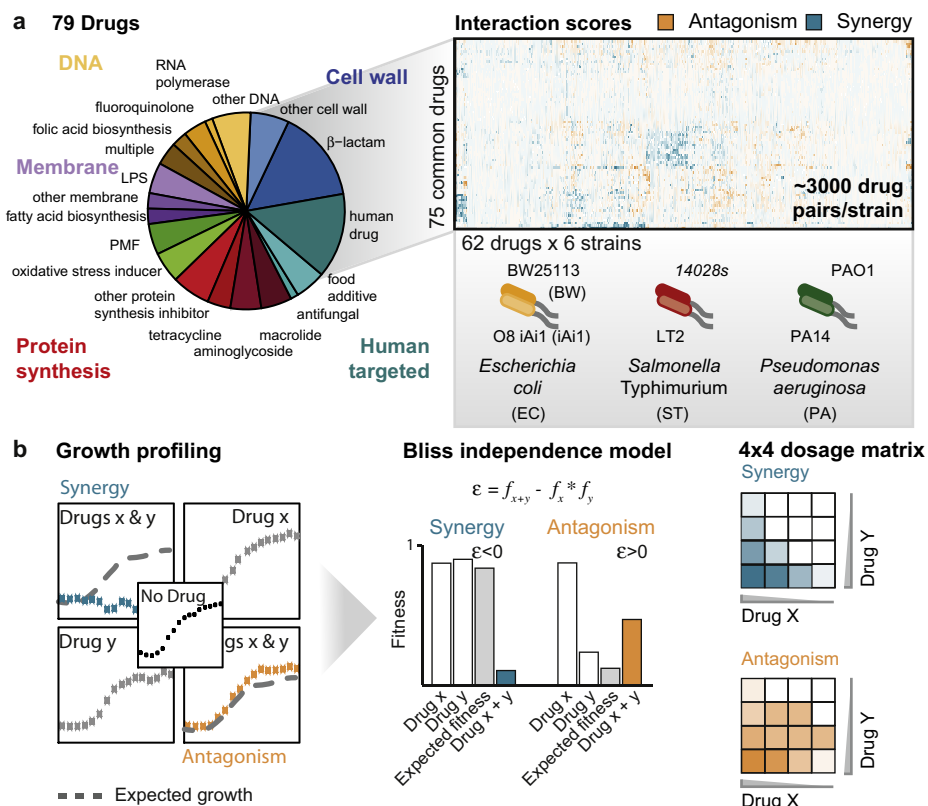
The *E. coli* Keio knockout collection²⁶ (two independent clones per mutant) was arrayed in 1,536-format on LB agar plates using a Rotor HDA (Singer Instruments) as previously described²⁹. The growth of each mutant was estimated by colony opacity⁴⁴ after a 13-h incubation at 37 °C in the absence and presence of vanillin (200 µg/ml), spectinomycin (4 µg/ml) and their combination. All plates were imaged under controlled lighting conditions (spImager, S&P Robotics) using an 18-megapixel Canon Rebel T3i (Canon). Experiments were done in biological triplicates. The fitness of each mutant was calculated by dividing the growth in condition (vanillin, spectinomycin or both) by the growth in LB, after correcting for outer-frame plate effects⁴⁴. Bliss scores were calculated according to equation (1) per replicate and then averaged (Supplementary Table 7).

Reporting summary. Further information on experimental design is available in the Nature Research Reporting Summary linked to this paper.

Code availability. The code used for data analysis is available from <https://github.com/AraRitaBrochado/DrugInteractionsPipeline>.

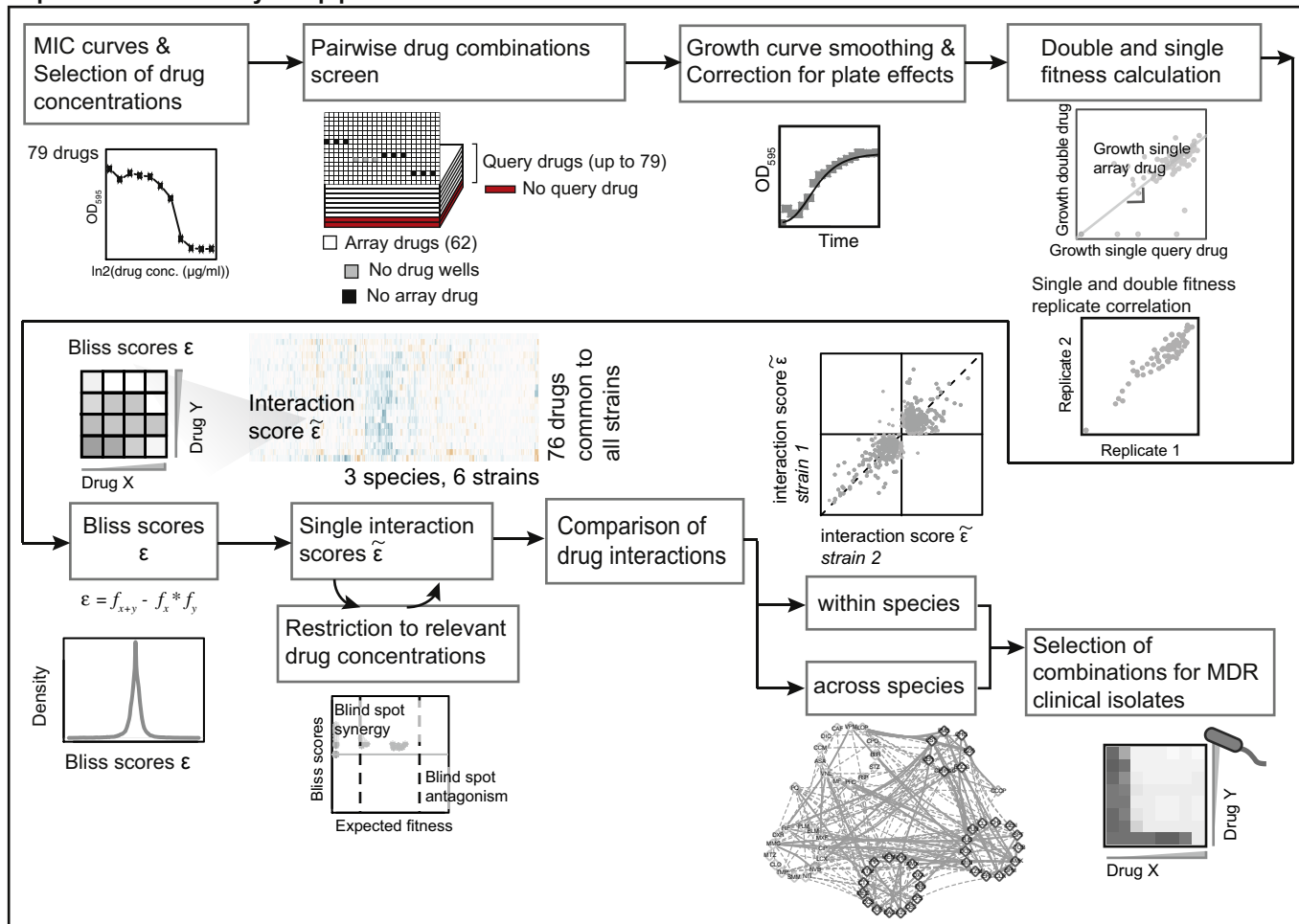
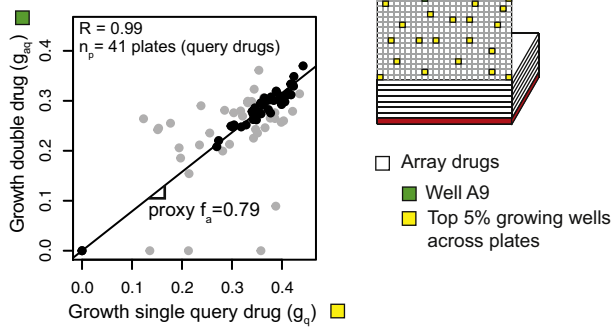
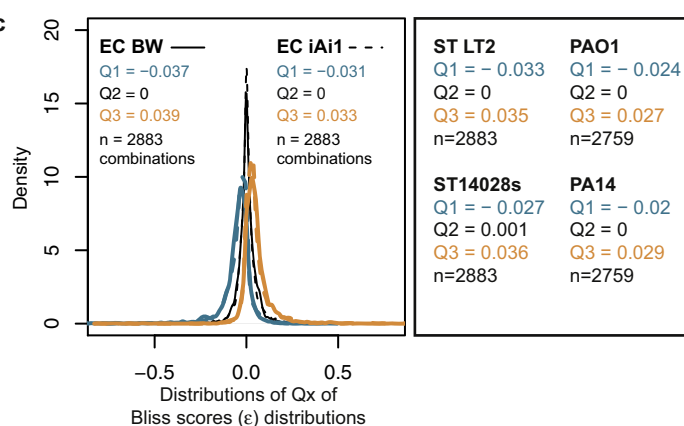
Data availability. All data supporting the findings of this study are included in this paper as Supplementary Information.

33. Datsenko, K. A. & Wanner, B. L. One-step inactivation of chromosomal genes in *Escherichia coli* K-12 using PCR products. *Proc. Natl Acad. Sci. USA* **97**, 6640–6645 (2000).
34. Saka, K. et al. A complete set of *Escherichia coli* open reading frames in mobile plasmids facilitating genetic studies. *DNA Res.* **12**, 63–68 (2005).
35. Shannon, P. et al. Cytoscape: a software environment for integrated models of biomolecular interaction networks. *Genome Res.* **13**, 2498–2504 (2003).
36. Yeh, P. J., Hegreness, M. J., Aiden, A. P. & Kishony, R. Drug interactions and the evolution of antibiotic resistance. *Nat. Rev. Microbiol.* **7**, 460–466 (2009).
37. Bliss, C. I. The toxicity of poisons applied jointly. *Ann. Appl. Biol.* **26**, 585–615 (1939).
38. Loewe, S. Die quantitativen Probleme der Pharmakologie. *Ergeb. Physiol.* **27**, 47–187 (1928).
39. Szappanos, B. et al. An integrated approach to characterize genetic interaction networks in yeast metabolism. *Nat. Genet.* **43**, 656–662 (2011).
40. Mateus, A. et al. Prediction of intracellular exposure bridges the gap between target- and cell-based drug discovery. *Proc. Natl Acad. Sci. USA* **114**, E6231–E6239 (2017).
41. Richter, M. F. et al. Predictive compound accumulation rules yield a broad-spectrum antibiotic. *Nature* **545**, 299–304 (2017).
42. Piddock, L. J., Jin, Y. F., Ricci, V. & Asuquo, A. E. Quinolone accumulation by *Pseudomonas aeruginosa*, *Staphylococcus aureus* and *Escherichia coli*. *J. Antimicrob. Chemother.* **43**, 61–70 (1999).
43. Livak, K. J. & Schmittgen, T. D. Analysis of relative gene expression data using real-time quantitative PCR and the 2^{-ΔΔCt} method. *Methods* **25**, 402–408 (2001).
44. Kritikos, G. et al. A tool named Iris for versatile high-throughput phenotyping in microorganisms. *Nat. Microbiol.* **2**, 17014 (2017).
45. Safdar, N., Handelsman, J. & Maki, D. G. Does combination antimicrobial therapy reduce mortality in Gram-negative bacteraemia? A meta-analysis. *Lancet Infect. Dis.* **4**, 519–527 (2004).
46. Taber, H. W., Mueller, J. P., Miller, P. F. & Arrow, A. S. Bacterial uptake of aminoglycoside antibiotics. *Microbiol. Rev.* **51**, 439–457 (1987).
47. Mazzariol, A., Tokue, Y., Kanegawa, T. M., Cornaglia, G. & Nikaido, H. High-level fluoroquinolone-resistant clinical isolates of *Escherichia coli* overproduce multidrug efflux protein AcrA. *Antimicrob. Agents Chemother.* **44**, 3441–3443 (2000).
48. Davis, B. D., Chen, L. L. & Tai, P. C. Misread protein creates membrane channels: an essential step in the bactericidal action of aminoglycosides. *Proc. Natl Acad. Sci. USA* **83**, 6164–6168 (1986).
49. Miller, P. F., Gambino, L. F., Sulavik, M. C. & Gracheck, S. J. Genetic relationship between *soxRS* and *mar* loci in promoting multiple antibiotic resistance in *Escherichia coli*. *Antimicrob. Agents Chemother.* **38**, 1773–1779 (1994).
50. Fernandes, F., Neves, P., Gameiro, P., Loura, L. M. & Prieto, M. Ciprofloxacin interactions with bacterial protein OmpF: modelling of FRET from a multi-tryptophan protein trimer. *Biochim. Biophys. Acta* **1768**, 2822–2830 (2007).
51. Machado, D. et al. Ion channel blockers as antimicrobial agents, efflux inhibitors, and enhancers of macrophage killing activity against drug resistant *Mycobacterium tuberculosis*. *PLoS ONE* **11**, e0149326 (2016).
52. Maier, L. et al. Extensive impact of non-antibiotic drugs on human gut bacteria. *Nature* **555**, 623–628 (2018).



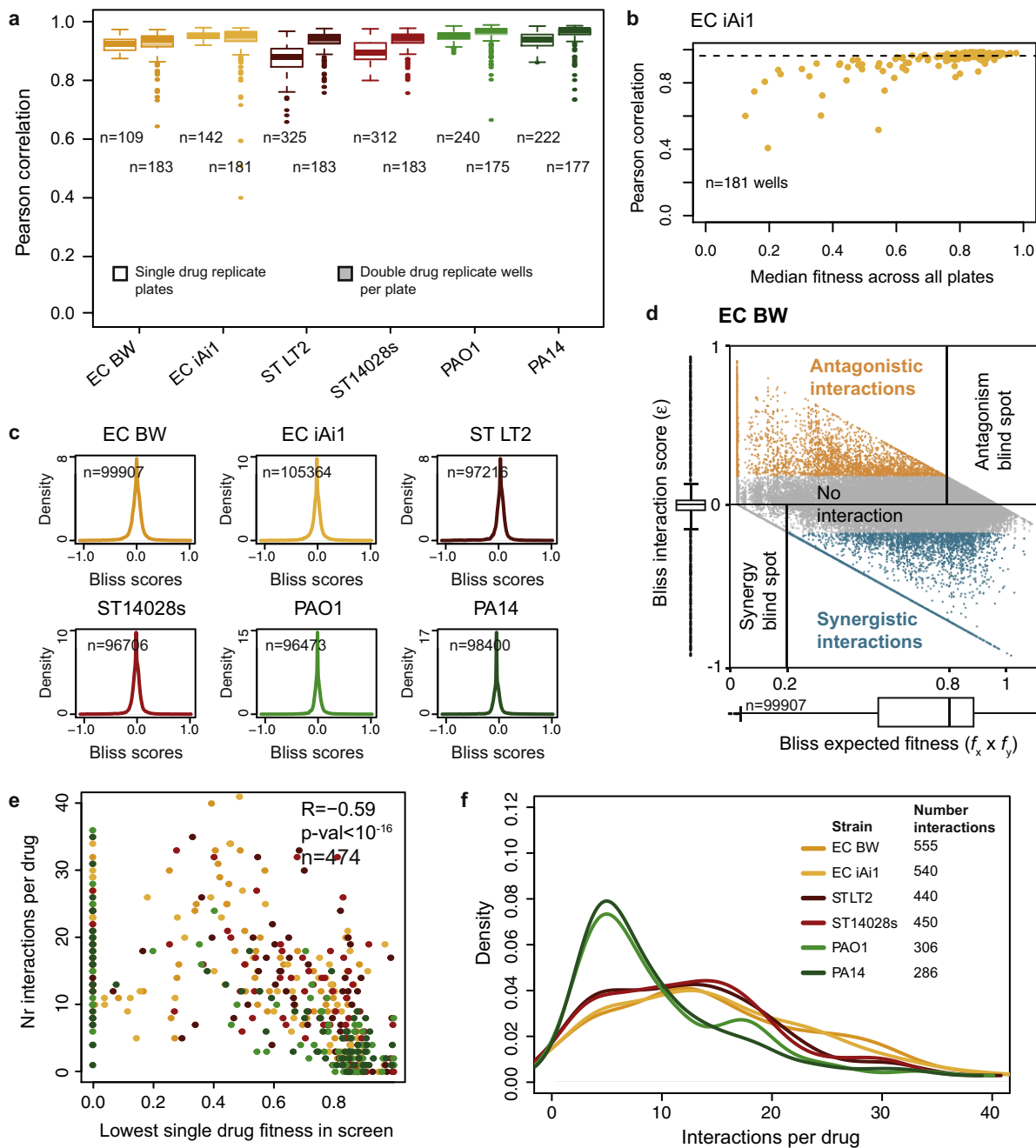
Extended Data Fig. 1 | High-throughput profiling of pairwise drug combinations in Gram-negative bacteria. **a**, Drug and species selection for screen. The 79 drugs used in the combinatorial screen are grouped according to categories (Supplementary Table 1). Antibacterial agents are grouped by target, with the exception of antibiotic classes for which enough representatives were screened (>2) to form a separate category (β -lactams, macrolides, tetracyclines, fluoroquinolones and aminoglycosides). Classification of human-targeted drugs and food additives is not further refined, because for most of these the mode of action is unclear. A subset of 62 arrayed drugs was profiled against

79 drugs in all 6 strains (75 drugs were common to all strains and are depicted in the heat map). Strains are colour-coded according to species: yellow, *E. coli*; red, *S. Typhimurium*; green, *P. aeruginosa*. **b**, Quantification of drug–drug interactions. Growth was profiled by measuring optical density ($OD_{595\text{ nm}}$) over time in the presence of no, one and both drugs. x and y correspond to particular concentrations of drugs X and Y . Interactions were defined according to Bliss independence. Significantly lower or higher fitness than the expectation ($f_x \times f_y$) indicates synergy or antagonism, respectively. Synergy and antagonism were assessed by growth in 4×4 checkerboards (Methods).

a**Experimental and analytical pipeline****b Well A9: EC BW**Array drug: spectinomycin 3 $\mu\text{g/ml}$ **c**

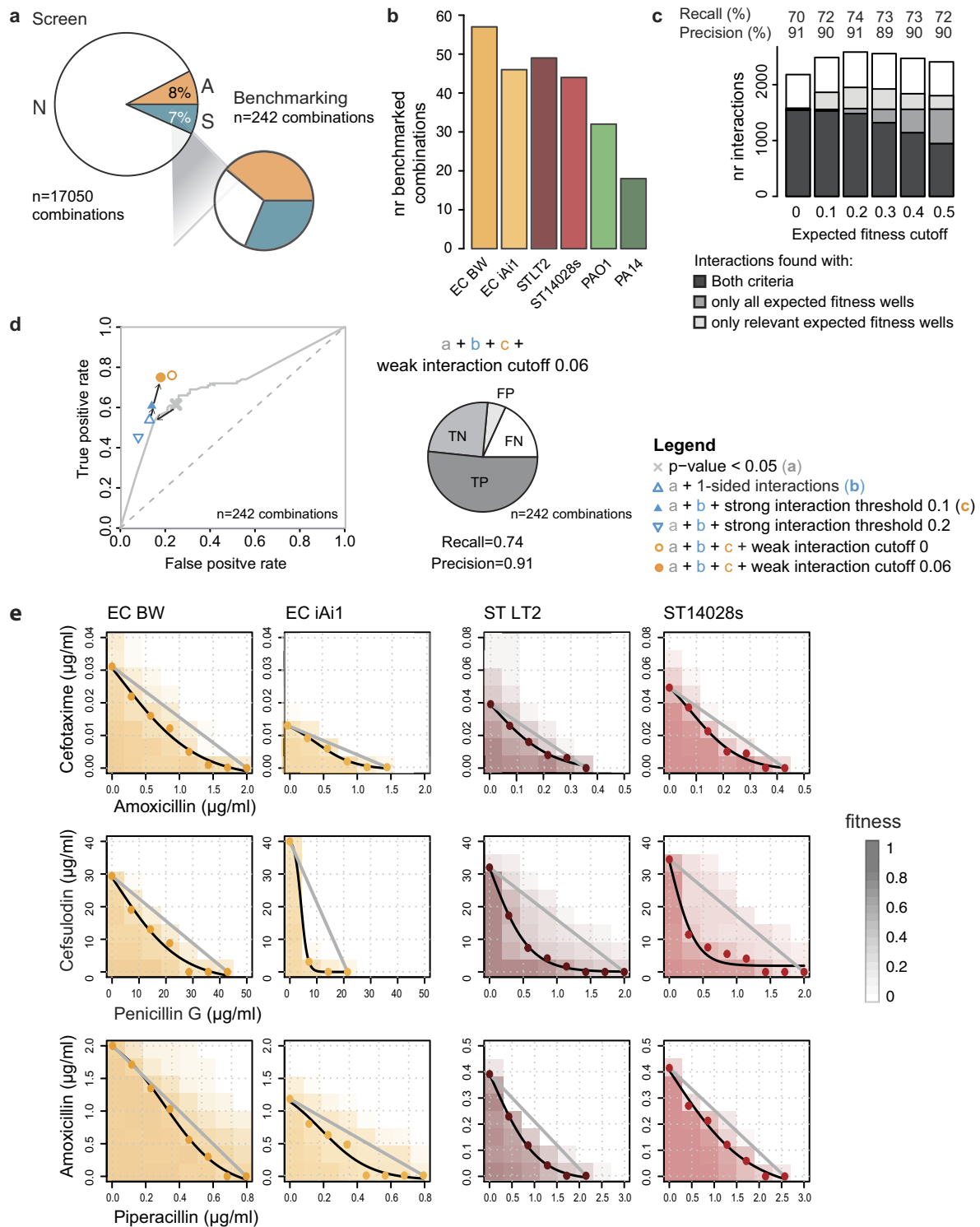
Extended Data Fig. 2 | Data analysis pipeline. **a**, Flowchart of the data analysis pipeline. **b**, Estimating single-drug fitness of arrayed drugs. As drug–drug interactions are rare, the slope of the line of best fit between g_{aq} (growth with double drug) and g_q (growth with query drug alone, which was deduced from the average of the top 5% growing wells across plates within a batch), across plates (n_p) of query drugs within a batch, corresponds to a proxy of the fitness of the arrayed drug alone, f_a (see Methods). r denotes the Pearson correlation coefficient between g_{aq} and g_q across n_p . Well A9 from *E. coli* BW25113, containing 3 $\mu\text{g ml}^{-1}$

spectinomycin, is shown as an example of arrayed drugs with several interactions. Several query drugs deviated from the expected fitness (light grey points), and therefore only half of the plates corresponding to the interquartile range of g_{aq}/g_q were used to estimate f_a . **c**, Density distributions of the first, second and third quartiles of Bliss-score (ε) distributions for *E. coli*. Q_1 , Q_2 and Q_3 denote the median of the first, second and third quartiles of ε distributions, respectively. n denotes the number of drug combinations used.



Extended Data Fig. 3 | Data quality control. **a**, High replicate correlation for single- and double-drug treatments. Transparent box plots contain Pearson correlation coefficients between plates of the same batch that contain only arrayed drugs (for which LB was used instead of the second drug). n represents the total number of correlations. Full box plots contain Pearson correlation coefficients between double-drug replicate wells within the same plate, across all plates. n represents the number of wells used for correlation, $n_{\max} = (62 \text{ drugs} + 1 \text{ LB}) \times 3 \text{ concentrations} = 189$. Only wells with median growth above 0.1 were taken into account for this correlation analysis (see **b**). For all box plots the centre line, limits, whiskers and points correspond to the median, upper and lower quartiles, $1.5 \times$ interquartile range and outliers, respectively. **b**, Wells with lower median growth have lower replicate correlation. The double-drug correlation coefficients used to generate the box plot from **a** are plotted as a function of the median growth of all wells across all plates for *E. coli* iAi1. Wells with overall lower growth (due to the strong inhibition of the arrayed drug) are less reproducible owing to a combination of the lower spread of growth values and the sigmoidal nature of the drug–dose response curves. **c**, Drug–drug interactions are rare. Density distributions

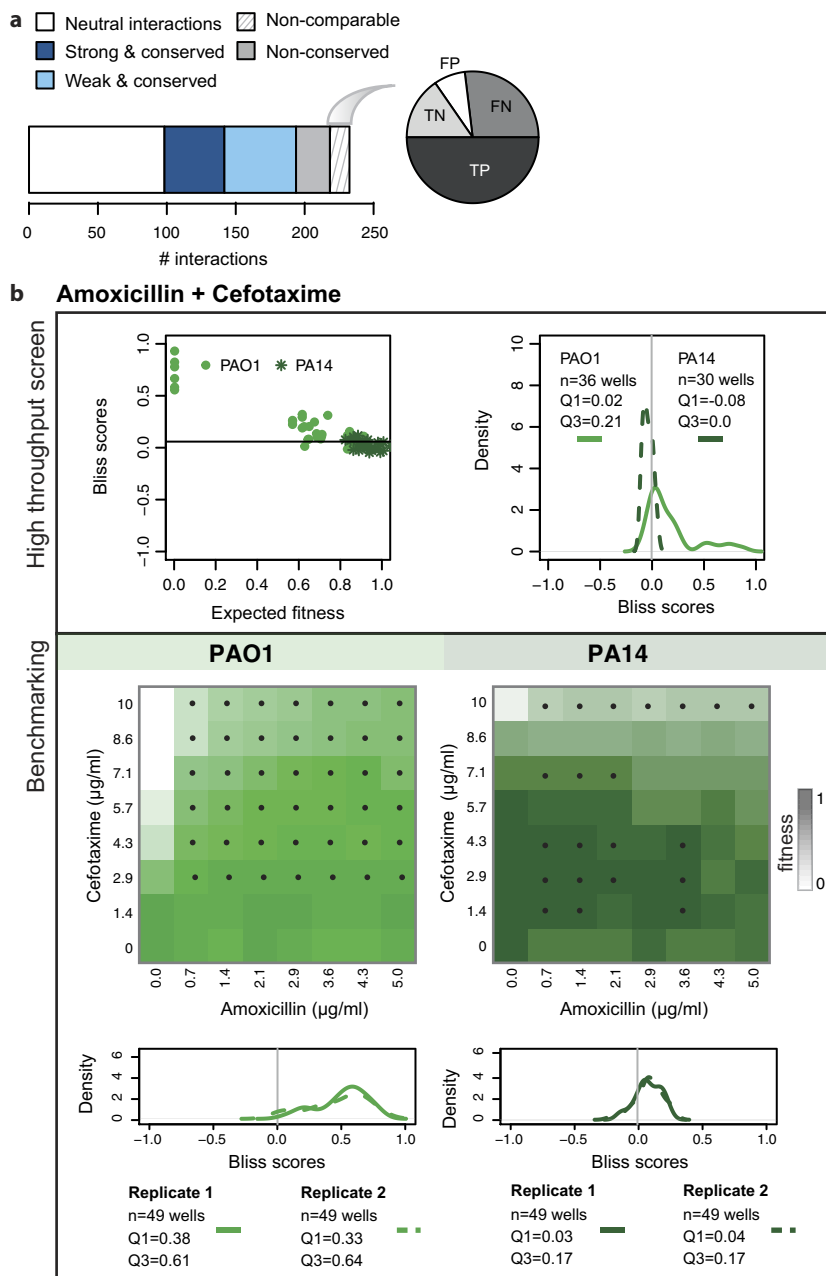
of all Bliss scores (ε) obtained per strain. **d**, The ability to detect synergies and antagonisms depends on the effects of single-drug treatments. Bliss scores (ε) are plotted as function of expected fitness ($f_x \times f_y$) for all drug concentration ratios for all combinations in *E. coli* BW25113 (as an example). Box plots summarizing both variables are shown besides the axes ($n = 99,907$ Bliss scores; centre line, limits, whiskers and points correspond to the median, upper and lower quartiles, $1.5 \times$ interquartile range and outliers, respectively). Blind spots for detecting antagonism and synergy are indicated; both of these are based on the expected fitness (see also Extended Data Fig. 4c, d), and are therefore dependent on the growth of the strain with the single drugs. The number of drug combinations falling in the blind spot for antagonism is larger, owing to the number of drugs used in the screen that do not inhibit *E. coli* on their own. **e**, Scatter plot of the number of interactions per drug versus the minimum fitness of the drug alone (as obtained in the screen, Supplementary Table 1). Strong and weak interactions are represented. n denotes the total number of interactions and r is the Pearson correlation coefficient. Strains are colour-coded as above. **f**, Density distributions of the number of interactions per drug for all strains.



Extended Data Fig. 4 | See next page for caption.

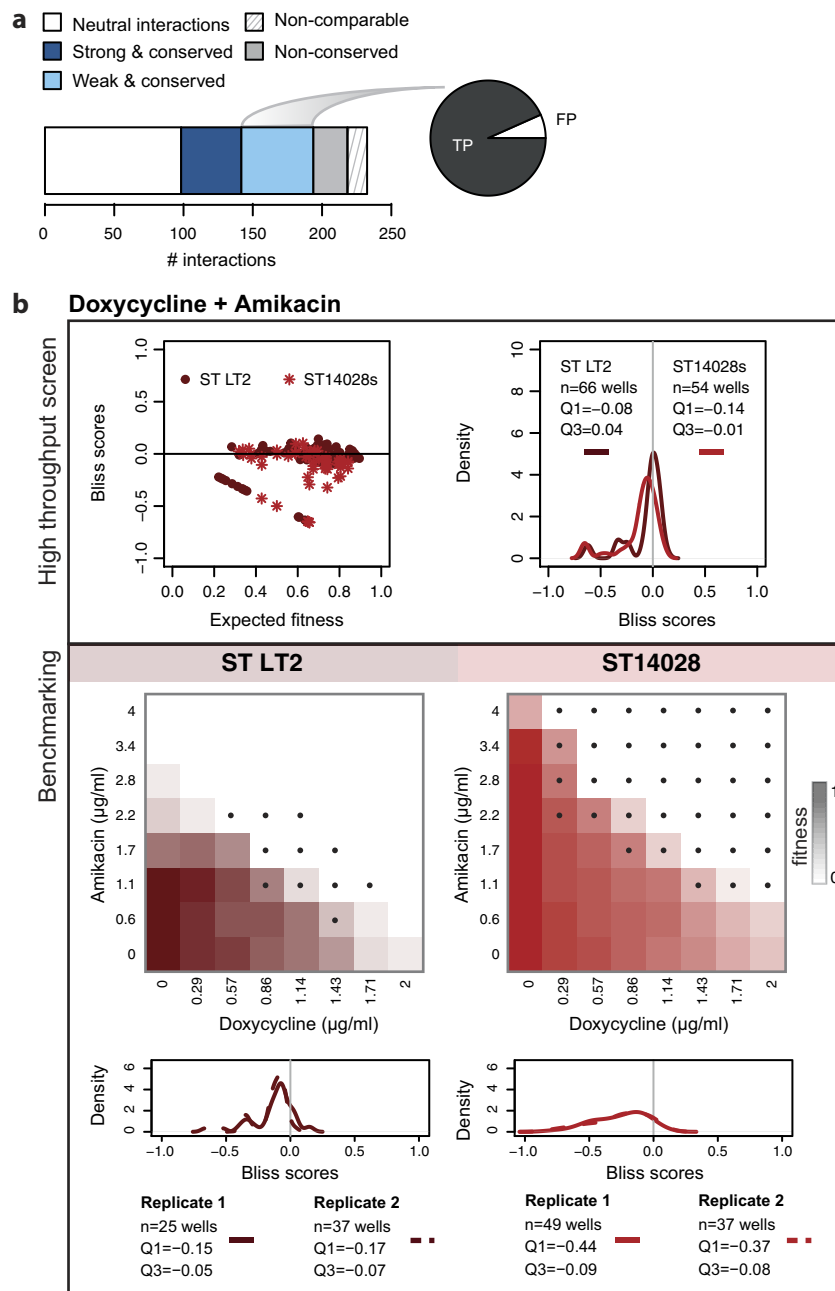
Extended Data Fig. 4 | Benchmarking and sensitivity analysis. **a**, The validation set is enriched in synergies and antagonisms to better assess true and false positives. Comparison of percentages of synergy and antagonism between the screen and validation set. Both strong and weak interactions (Fig. 2b) are accounted for in the screen tally. **b**, Number of benchmarked interactions per strain. **c, d**, Sensitivity analysis of the statistical thresholds for calling interactions. **c**, The total number of interactions as a function of the expected fitness ($f_x \times f_y$) cutoff was used to restrict the ε distributions to relevant drug concentrations. Strong drug–drug interactions are classified according to the ε distribution in which they were significant: complete distribution only (that is, all expected fitness wells), relevant wells only (that is, all wells with $f_x \times f_y >$ cutoff for synergies and all wells with $f_x \times f_y < (1 - \text{cutoff})$ for antagonisms), or in both. Weak drug–drug interactions are independently assigned and represented in white. We selected an expected fitness cutoff of 0.2, as this cutoff resulted in the largest number of total interactions detected, with the highest precision and recall (91 and 74%, respectively) after benchmarking against the validation dataset. **d**, Receiver operating characteristic curve for the screen across different P value thresholds (10,000 repetitions of a two-sided permutation test of Wilcoxon rank-sum test after correction for multiple

testing, see Methods) as a unique criterion for assigning interactions. The selected P value (0.05) for the screen threshold is indicated by a grey cross. Sensitivity to additional parameters for calling hits is shown: allowing interactions to be either antagonisms or synergies but not both (one-sided); as well as strong and weak interaction thresholds. True- and false-positive rates were estimated based on the validation dataset. Precision and recall for the final and best-performing set of parameters are shown: one-sided interactions, $P < 0.05$, $f_x \times f_y$ cutoff = 0.2 and $|\varepsilon| > 0.1$ for strong interactions, $|\varepsilon| > 0.06$ for weak interactions. TP, true positive; TN, true negative; FP, false positive; FN, false negative. n indicates the total number of benchmarked drug combinations (Supplementary Table 3). **e**, Synergies between β -lactams according to the Loewe additivity interaction model. The results of 8×8 checkerboards for 3 combinations between β -lactams in 4 strains are shown. The grey line in each plot represents the null hypothesis in the Loewe additivity model and the black line corresponds to the IC_{50} isobole, which was estimated by fitting a logistic curve to the interpolated drug concentrations (coloured dots, Methods). Piperacillin did not reach 50% growth inhibition in *E. coli*, thus IC_{20} and IC_{40} isoboles were used for the amoxicillin + piperacillin combination in *E. coli* BW25113 and *E. coli* IAI1, respectively.



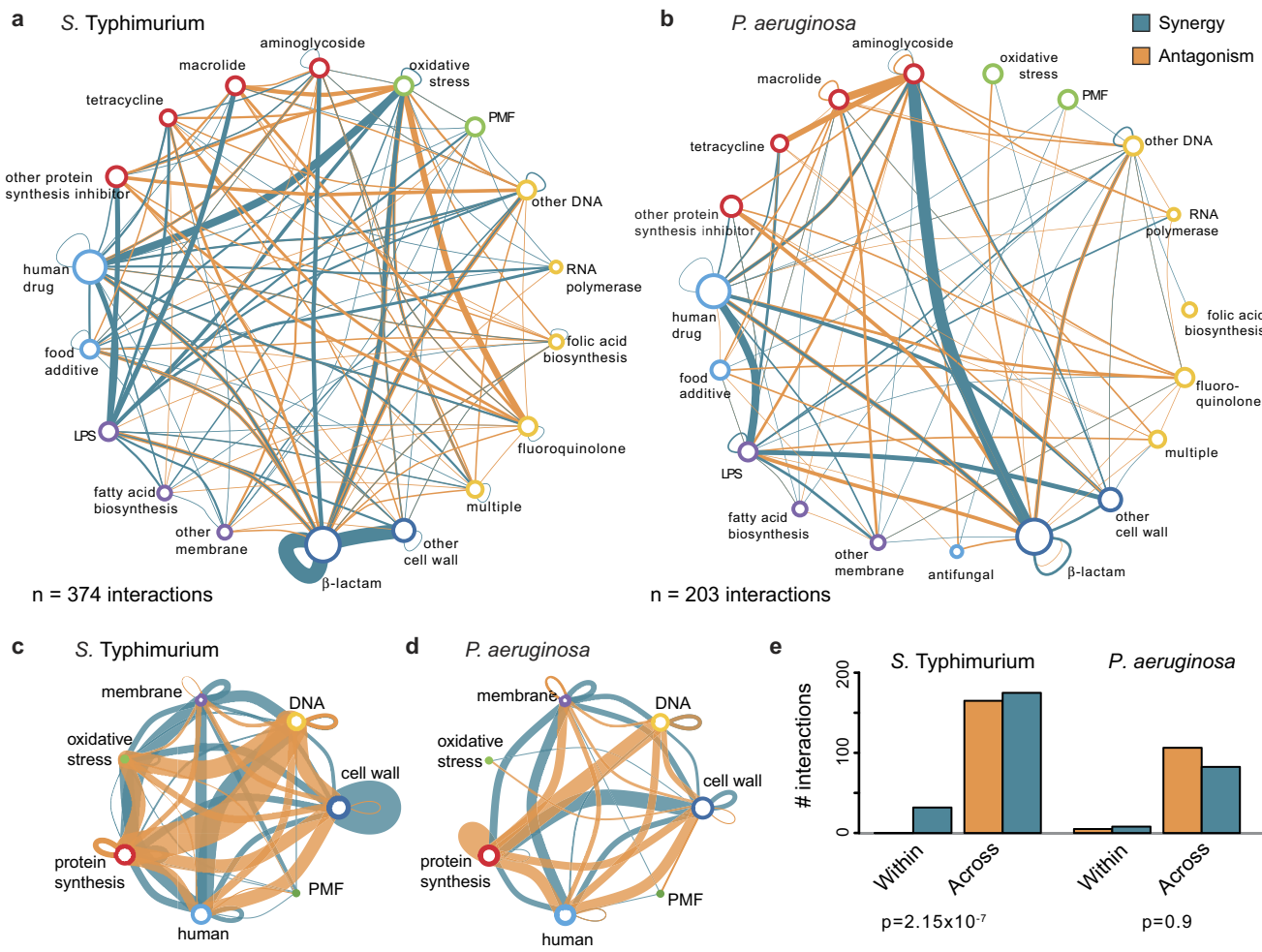
Extended Data Fig. 5 | Benchmarking of non-comparable drug-drug interactions. **a**, The bar plot illustrates the division of benchmarked drug combinations according to their degree of conservation within species. The pie chart shows the proportion of false positives (FP), true positives (TP), false negatives (FN) and true negatives (TN) within non-comparable drug-drug interactions. **b**, Combination of amoxicillin with cefotaxime in *P. aeruginosa* as an example of a non-comparable drug-drug interaction. Top box, the results of the screen. Left, Bliss scores as function of expected fitness for both strains. Right, a density distribution

of the Bliss scores. n denotes the total number of Bliss scores, Q1 and Q3 indicate the Bliss score for the first and third quartiles, respectively. Antagonism was detected only for PAO1 ($Q3 > 0.1$). PA14 was resistant to both drugs at concentrations screened (top left panel), rendering the detection of antagonism impossible. Bottom box, benchmarking results indicate that the interaction is antagonistic in both strains, albeit weaker in PA14 and visible mostly at higher concentrations. The colour intensity on checkerboard reflects fitness and black dots correspond to drug ratios in which the Bliss score is above 0.1.



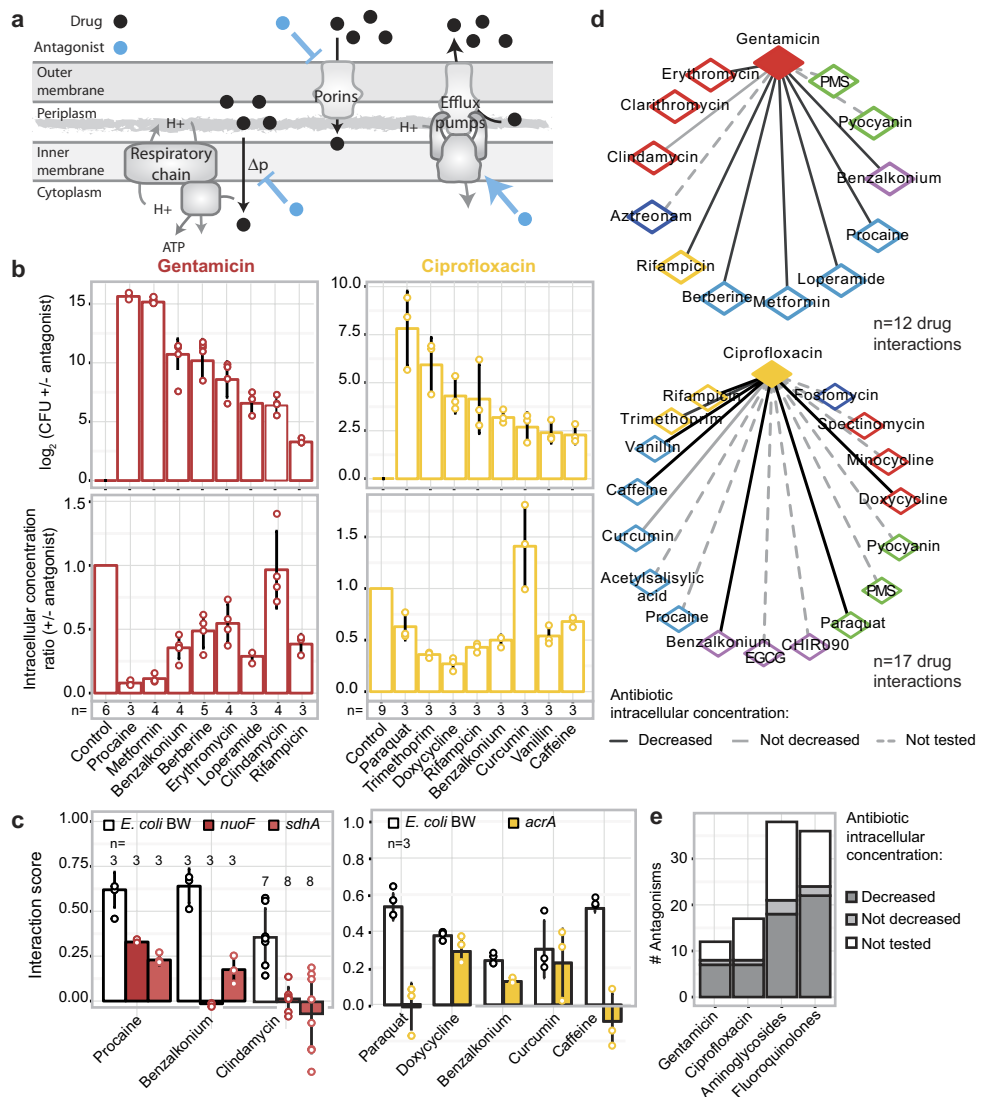
Extended Data Fig. 6 | Benchmarking of weak conserved drug–drug interactions. **a**, The bar plot illustrates the division of benchmarked drug combinations as in Extended Data Fig. 5a. The pie chart shows the proportion false positives and true positives within weak conserved interactions. **b**, Combination of doxycycline with amikacin in *S. Typhimurium* as an example of a weak conserved drug–drug interaction. Top box, the results of the screen. Left, Bliss scores as a function of expected fitness for both strains. Right, a density distribution of the Bliss

scores. n denotes the total number of Bliss scores, Q1 and Q3 indicate the Bliss score for quartiles 1 and 3, respectively. A strong synergy was detected only for ST14028 ($Q1 < -0.1$), and a weak conserved synergy was assigned afterwards to ST LT2 ($Q1 < -0.06$). Bottom box, the benchmarking results confirm that the interaction is synergistic in both strains. The colour intensity on checkerboard reflects fitness and black dots correspond to drug ratios in which the Bliss score is below -0.1 .



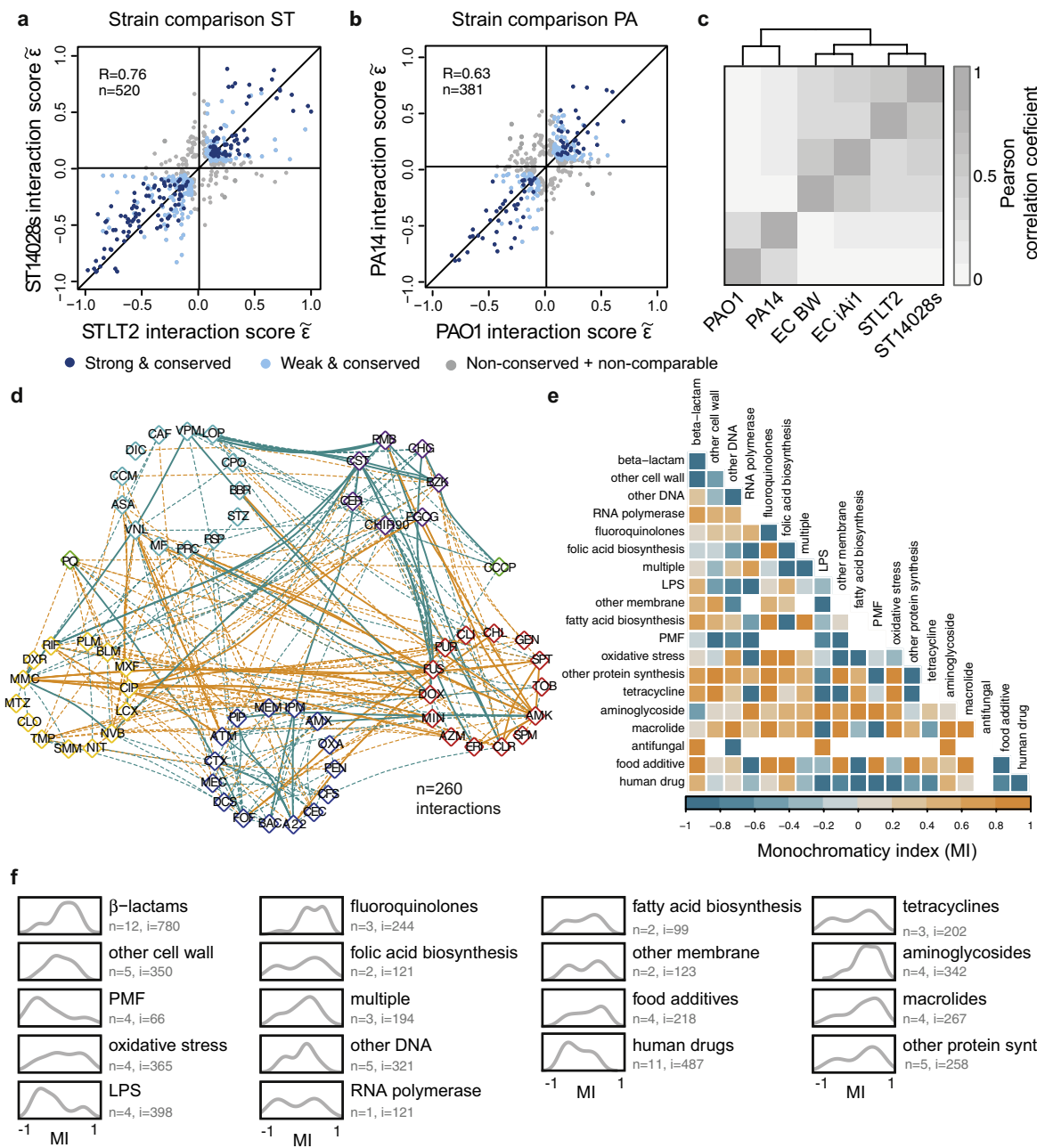
Extended Data Fig. 7 | Salmonella and Pseudomonas drug–drug interaction networks. **a, b**, Drug category interaction networks. Nodes represent drug categories according to Extended Data Fig. 1a, and plotted as in Fig. 1b. Conserved interactions, including weak conserved interactions, are shown here. One of the most well-known and broadly used synergies is that of aminoglycosides and β -lactams⁴⁵. Consistent with its use against *P. aeruginosa* in clinics, we detected multiple strong synergies between specific members of the two antibiotic classes in *P. aeruginosa* but fewer interactions in the other two species.

c, d, Drug–drug interactions across cellular processes. Representation as in **a, b** but grouping drug categories targeting the same general cellular process. **e**, Quantification of synergy and antagonism in the networks from **a, b** and the corresponding χ^2 -test *P* value. As in *E. coli* (Fig. 1), antagonism occurs more frequently than synergy and almost exclusively between drugs belonging to different categories in *S. Typhimurium* and *P. aeruginosa*. In *P. aeruginosa*, there are very few interactions occurring between drugs of the same category (within the group).



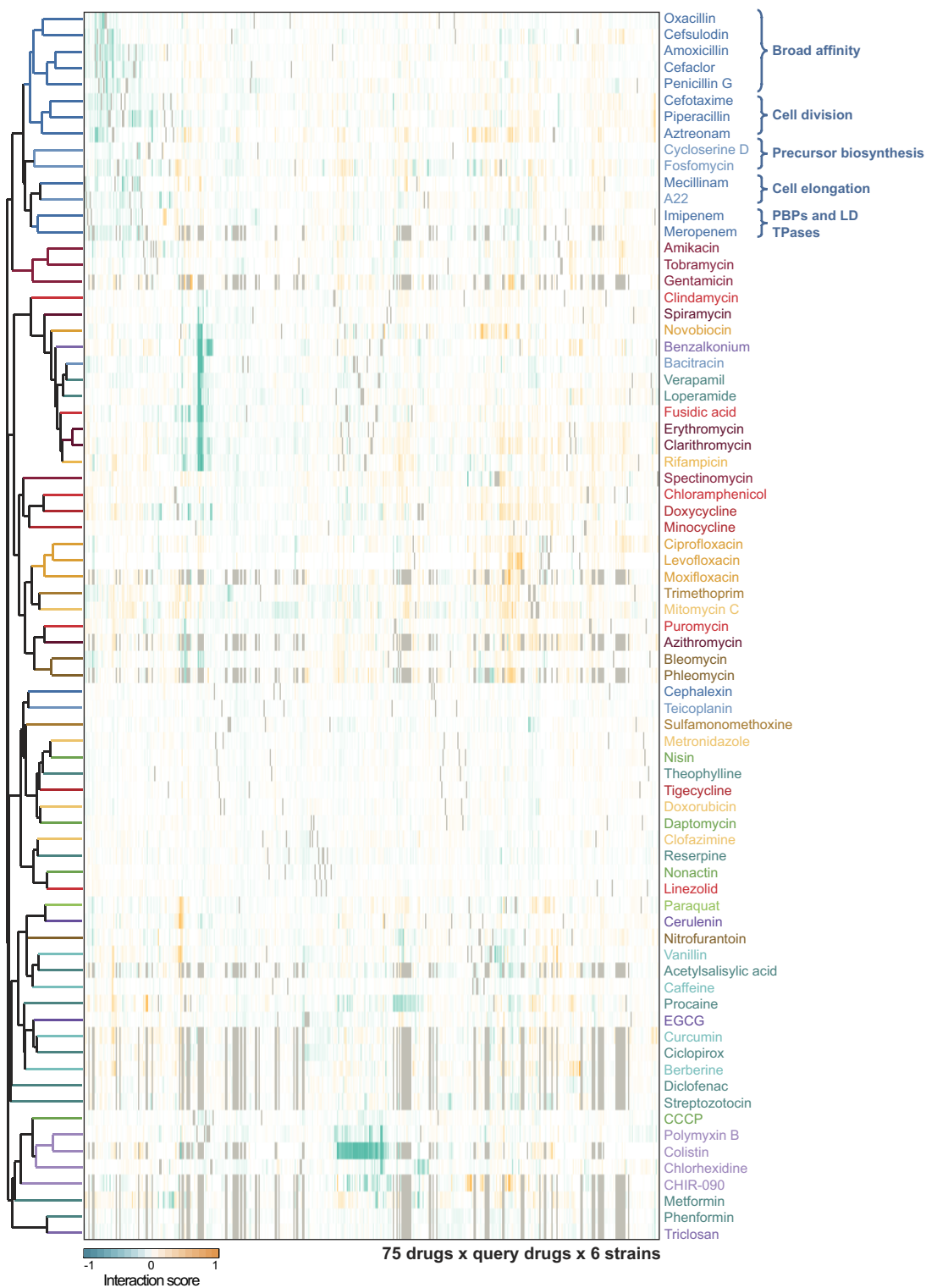
Extended Data Fig. 8 | Drug antagonisms are often due to a decrease in intracellular drug concentrations. **a**, Cartoon of possible modes of action for drug–drug interactions that function via modulation of the intracellular drug concentration. A given drug (antagonist, blue) inhibits the uptake or promotes the efflux of another drug (black), and thus decreases its intracellular concentration. **b**, Different antagonists (see Methods for concentrations) of gentamicin (red, 5 $\mu\text{g ml}^{-1}$) and ciprofloxacin (yellow, 2.5 $\mu\text{g ml}^{-1}$) identified in our screen for *E. coli* BW25113 also rescue the killing effect of the two bactericidal drugs in the same strain, or its parental MG1655 (top right and top left panels, respectively). With the exception of clindamycin (for gentamicin) and curcumin (for ciprofloxacin), all other antagonists decrease the intracellular concentration of their interacting drug (bottom panels). Gentamicin was detected by using radiolabelled compound, and ciprofloxacin with LC–MS/MS (Methods). The degree of rescue (top panels) in many cases follows the decrease in intracellular concentration (bottom panels), which implies that most of these interactions depend at least partially on modulating the intracellular concentration of the antagonized drug. **c**, Antagonisms are resolved in *E. coli* BW25113 mutants that lack key components that control the intracellular concentration of the antagonized drug. Aminoglycosides depend on proton motive force-energized uptake, and thus on respiratory complexes^{7,46}; ciprofloxacin is effluxed by AcrAB–TolC^{29,47}. For gentamicin, most interactions are resolved when respiration is defected, even the interaction with clindamycin (which does not modulate intracellular gentamicin concentration, see **b**); this presumably occurs because the mode of action and import of aminoglycosides are linked by a positive feedback

loop^{7,48}. For ciprofloxacin, antagonisms with paraquat and caffeine are resolved in the ΔacrA mutant, which implies that both compounds induce the AcrAB–TolC pump (well-established for paraquat⁴⁹). By contrast, interactions with curcumin, benzalkonium and doxycycline remain largely intact in the ΔacrA mutant. The first interaction is expected, as curcumin does not modulate intracellular ciprofloxacin concentration (see **b**). In the other two cases, other component(s) besides AcrAB–TolC may be responsible for the altered ciprofloxacin import and/or export; for example, ciprofloxacin uses OmpF to enter the cell⁵⁰. Ciprofloxacin and gentamicin concentrations were adjusted in all strains according to MIC (70% and 100% MIC for ciprofloxacin and gentamicin, respectively; all drug concentrations are listed in Supplementary Table 6). Bliss interaction scores (ε) were calculated as in the screen. Bar plots and error bars in **b**, **c** represent the average and s.d., respectively, across n independent biological replicates. **d**, Gentamicin and ciprofloxacin antagonism networks for *E. coli* BW. Nodes represent drugs coloured according to targeted cellular process (as in Extended Data Fig. 1a). Full and dashed edges represent antagonistic drug–drug interactions for which intracellular antibiotic concentration was and was not measured, respectively. Drug interactions that result in decreased intracellular concentration of the antagonized drug are represented by black edges. **e**, Quantification of antagonistic drug–drug interactions from the networks in **d**. The bars for fluoroquinolones and aminoglycosides account for an extrapolation of antagonistic interactions to all other members of the two classes, assuming that they behave in the same way as ciprofloxacin and gentamicin, respectively.



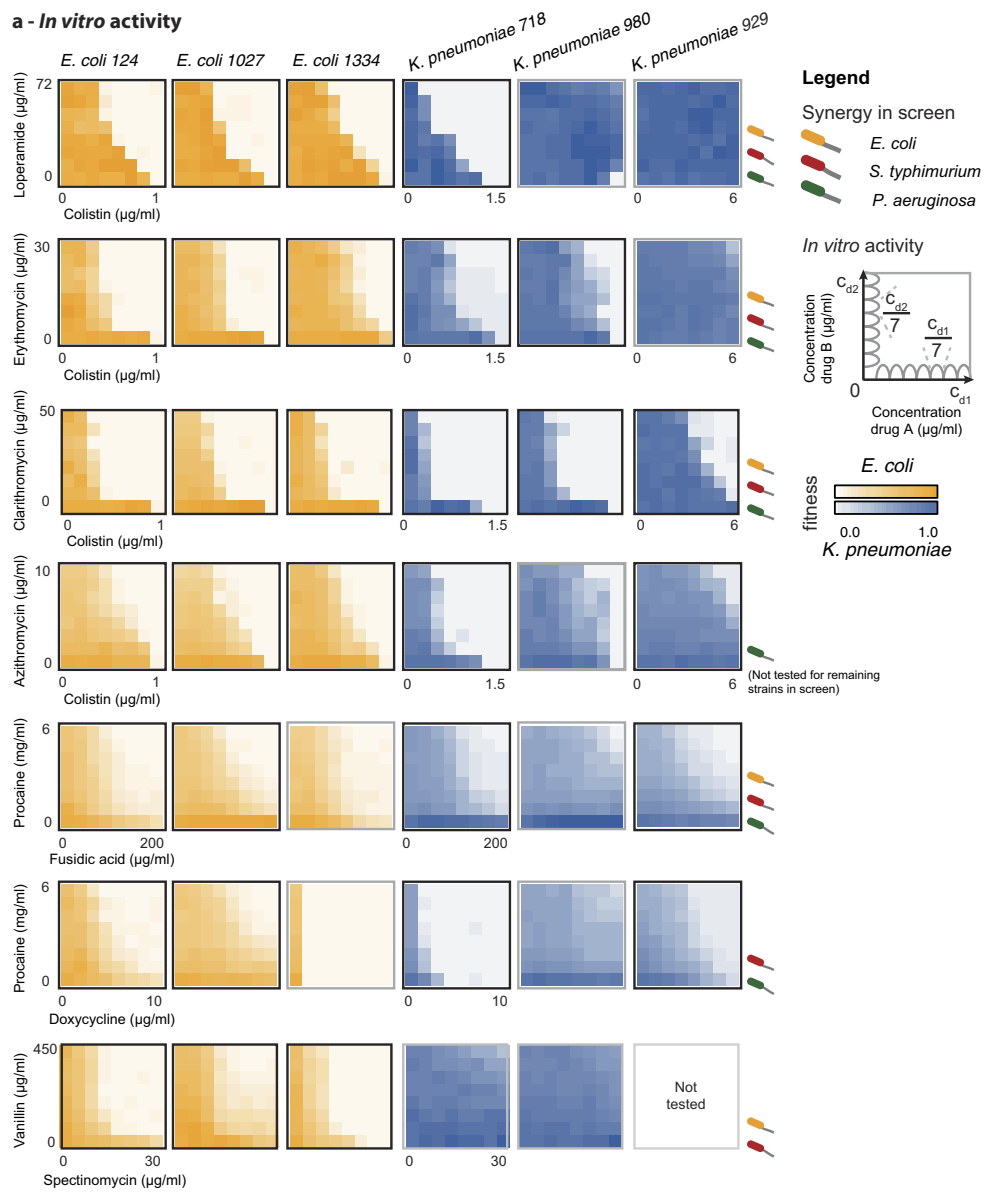
Extended Data Fig. 9 | Drug–drug interactions are largely conserved within species and only partially driven by mode of action. **a, b**, Drug–drug interactions are conserved in *S. Typhimurium* (a) and *P. aeruginosa* (b). Scatter plot of interaction scores in the two strains of each species; only strong interactions for at least one strain are shown. Colours and grouping as in Fig. 2a. r denotes the Pearson correlation and n denotes the total number interactions plotted. The lower correlation in *P. aeruginosa* is presumably due to fewer and weaker interactions. **c**, Drug interaction profiles are driven by phylogeny. Clustering of strains based on the Pearson correlation of their drug interaction profiles (taking into account all pairwise drug combinations; $n = 2,759\text{--}2,883$ depending on the species). Strains of the same species cluster together; the two enterobacterial species—*E. coli* and *S. Typhimurium*—behave more similarly to one another than either does to the phylogenetically more-distant *P. aeruginosa*. **d**, Conserved drug–drug interaction network. Nodes represent individual drugs grouped and coloured by targeted cellular process (as in Extended Data Fig. 1a). Drug names are represented by three-letter codes (given in Supplementary Table 1). Dashed and full edges correspond to conserved interactions between two or three species, respectively. Many of the human-targeted drugs, such as loperamide,

verapamil and procaine, exhibit a general potentiating effect that is similar to that of membrane-targeting drugs. This suggests that these drugs may also facilitate drug uptake or impair efflux, consistent with previous reports on the role of loperamide in *E. coli* and verapamil in *Mycobacterium tuberculosis*^{4,51}. **e**, Monochromaticity between all drug categories. The monochromaticity index (MI) reflects whether interactions between drugs of two categories are more synergistic (MI = −1) or antagonistic (MI = 1) than the background proportion of synergy and antagonism. The MI equals zero when interactions between two drug categories have the same proportion of synergy and antagonism as all interactions together (Methods). The MI was calculated using all interactions from the six strains for all category pairs that had at least two interactions. White cells in the heat map correspond to category pairs for which no (or an insufficient number of) interactions were observed. **f**, Human-targeted drugs, and LPS or proton motive force inhibitors, are strong and promiscuous adjuvants. Density distributions of the monochromaticity indices per drug category from e are shown. n denotes the number of drugs in each category and i the number of interactions in which they are involved.



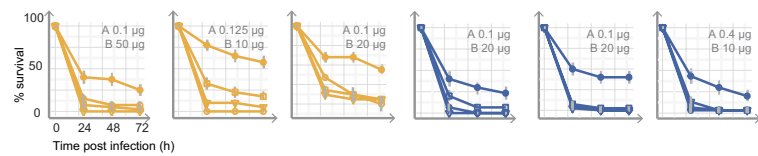
Extended Data Fig. 10 | Hierarchical clustering of drugs according to their interaction profiles. Rows depict the 75 drugs common to all strains (coloured according to drug category, see Extended Data Fig. 1a), and

columns depict their interactions with other drugs in all six strains tested. Clustering was done using the median of the ε distributions, uncentred correlation and average linkage.



b - *G. mellonella* infections

Drug A: Colistin **Drug B:** Clarithromycin



Drug A: Spectinomycin **Drug B:** Vanillin



Legend

G. mellonella infections

—○— No drug

□ Drug A

△ Drug B

● Drug A + Drug B

E. coli

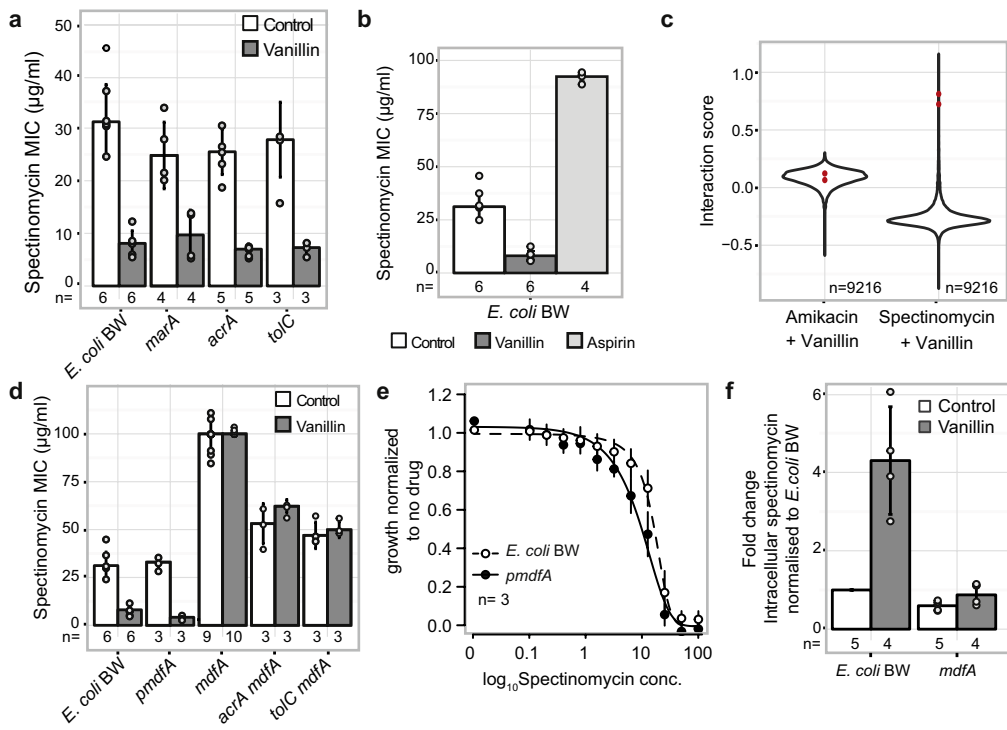
K. pneumoniae

Extended Data Fig. 11 | See next page for caption.

Extended Data Fig. 11 | Active synergies against Gram-negative MDR clinical isolates in vitro and in the *G. mellonella* infection model.

Both human-targeted drugs (which have recently been found to have an extended effect on bacteria⁵²) and food additives can promote the action of antibiotics in MDR strains, indicating that their use as antibacterial adjuvants should be explored further. **a**, Drug combinations active against MDR *E. coli* and *K. pneumoniae* clinical isolates (see also Fig. 4). Interactions are shown as 8×8 checkerboards and synergies have a black bold border. Drug pairs are the same for each row of panel **a**, and are indicated at the first checkerboard in each row. The species in which the interaction was detected in the screen are indicated after the last

checkerboard in each row. Concentrations increase in equal steps per drug (see legend); only minimal and maximal concentrations are shown for the first strain of each species. Apart from colistin, the same concentration ranges were used for all *E. coli* and *K. pneumoniae* MDR strains. One of two replicates is shown. **b**, Drug synergies against the same MDR strains in the *G. mellonella* infection model. Larvae were infected by *E. coli* and *K. pneumoniae* MDR isolates (10^6 and 10^4 CFUs, respectively) and left untreated, treated with single drugs or with the drug combination. The percentage of surviving larvae was monitored at indicated intervals after infection. $n = 10$ larvae per treatment. The averages of four biological replicates are plotted; error bars depict s.d.



Extended Data Fig. 12 | Mode of action for the vanillin–spectinomycin synergy. **a**, The spectinomycin MIC decreases upon addition of $100 \mu\text{g ml}^{-1}$ vanillin in the wild-type *E. coli* BW25113, as well as in *E. coli* single-gene knockouts of members of the AcrAB–TolC efflux pump or its MarA regulator. Thus, the vanillin–spectinomycin synergy is independent of the effect of vanillin on AcrAB–TolC (Fig. 3). **b**, Synergy is specific to vanillin–spectinomycin, as spectinomycin is antagonized by $500 \mu\text{g ml}^{-1}$ of the vanillin-related compound aspirin, thereby increasing the MIC by approximately threefold. **c**, Profiling the vanillin–spectinomycin combination in the *E. coli* BW Keio collection²⁶ to deconvolute its mode of action. Violin plots of the drug–drug interaction scores (ε) of all mutants ($n = 9,216$; Methods) are presented for the vanillin–spectinomycin combination (synergy) and, as control, for the combination of vanillin with another aminoglycoside amikacin (antagonism). The interaction scores of the two *mdfA* deletion clones present in the Keio library are indicated by red dots. The vanillin–spectinomycin synergy is lost in the absence of *mdfA* but the vanillin–amikacin antagonism remains unaffected, which indicates that the vanillin–spectinomycin synergy depends specifically on MdfA. **d**, Deletion of *mdfA* leads to an increased spectinomycin MIC and abolishes the synergy with vanillin, independent

of the presence or absence of AcrAB–TolC. Mild overexpression of *mdfA* from a plasmid (*pmdfA*, Methods) further enhances the synergy with vanillin, decreasing the spectinomycin MIC by about twofold (compared to the MIC of the combination in the wild type). **e**, Overexpression of *mdfA* leads to increased spectinomycin sensitivity, even though the MIC does not change. The growth of *E. coli* BW25113 carrying a plasmid with *mdfA* cloned in it (*pmdfA*; no inducer, mild overexpression) or the empty vector (BW) was measured ($\text{OD}_{595\text{ nm}}$ after 8 h) over twofold serial dilutions of spectinomycin and normalized to the no-drug growth of the corresponding strain (white and black dots represent the average of $n = 3$ independent biological replicates, error bars represent s.d.). The spectinomycin dose response was computed using a logistic fit of the averaged data points (MICs are calculated by fitting individual replicates, and then averaging). Fitted curves are represented by full and dashed lines for *pmdfA* and *E. coli* BW25113, respectively. **f**, Vanillin leads to accumulation of spectinomycin in the cell in an *mdfA*-dependent manner. Intracellular spectinomycin is measured with the tritiated compound (Methods). Bar plots and error bars in **a**, **b**, **d**, **f** represent the average and s.d., respectively, across n independent biological replicates.

Reporting Summary

Nature Research wishes to improve the reproducibility of the work that we publish. This form provides structure for consistency and transparency in reporting. For further information on Nature Research policies, see [Authors & Referees](#) and the [Editorial Policy Checklist](#).

Statistical parameters

When statistical analyses are reported, confirm that the following items are present in the relevant location (e.g. figure legend, table legend, main text, or Methods section).

n/a Confirmed

- The exact sample size (n) for each experimental group/condition, given as a discrete number and unit of measurement
- An indication of whether measurements were taken from distinct samples or whether the same sample was measured repeatedly
- The statistical test(s) used AND whether they are one- or two-sided
Only common tests should be described solely by name; describe more complex techniques in the Methods section.
- A description of all covariates tested
- A description of any assumptions or corrections, such as tests of normality and adjustment for multiple comparisons
- A full description of the statistics including central tendency (e.g. means) or other basic estimates (e.g. regression coefficient) AND variation (e.g. standard deviation) or associated estimates of uncertainty (e.g. confidence intervals)
- For null hypothesis testing, the test statistic (e.g. F , t , r) with confidence intervals, effect sizes, degrees of freedom and P value noted
Give P values as exact values whenever suitable.
- For Bayesian analysis, information on the choice of priors and Markov chain Monte Carlo settings
- For hierarchical and complex designs, identification of the appropriate level for tests and full reporting of outcomes
- Estimates of effect sizes (e.g. Cohen's d , Pearson's r), indicating how they were calculated
- Clearly defined error bars
State explicitly what error bars represent (e.g. SD, SE, CI)

Our web collection on [statistics for biologists](#) may be useful.

Software and code

Policy information about [availability of computer code](#)

Data collection

Provide a description of all commercial, open source and custom code used to collect the data in this study, specifying the version used OR state that no software was used.

Data analysis

Data analysis was performed in RStudio Version 1.0.136, using R version 2.15.1. Scripts deposited at <https://github.com/AnaRitaBrochado/DrugInteractionsPipeline>. Iris (doi:10.1038/nmicrobiol.2017.14) was used to process images of the *E. coli* gene knockout collection.

For manuscripts utilizing custom algorithms or software that are central to the research but not yet described in published literature, software must be made available to editors/reviewers upon request. We strongly encourage code deposition in a community repository (e.g. GitHub). See the Nature Research [guidelines for submitting code & software](#) for further information.

Data

Policy information about [availability of data](#)

All manuscripts must include a [data availability statement](#). This statement should provide the following information, where applicable:

- Accession codes, unique identifiers, or web links for publicly available datasets
- A list of figures that have associated raw data
- A description of any restrictions on data availability

All data generated during this study are included in this published article and its Supplementary Information files.

Field-specific reporting

Please select the best fit for your research. If you are not sure, read the appropriate sections before making your selection.

Life sciences Behavioural & social sciences Ecological, evolutionary & environmental sciences

For a reference copy of the document with all sections, see nature.com/authors/policies/ReportingSummary-flat.pdf

Life sciences study design

All studies must disclose on these points even when the disclosure is negative.

Sample size No prior assumptions were made regarding effect sizes.

Data exclusions Replicates with inconsistent growth behavior in the screen and validation dataset were excluded from our analysis. For follow up experiments, data exclusion was minimized to cases in which clear outliers due to technical mistakes were spotted. For noisy experiments, we increased the number of replicates.

Replication We have at least 4 replicates for each drug combination for the screen and present the reproducibility of the data in ED Fig. 3. We have at least 3 (in most times more) replicates for all follow up experiments, and data are always quantified and measurement error is presented. We benchmark our screen against an independently generated validation dataset. For higher resolution checkerboards used for validation experiments and for testing MDR strains, two independent biological replicates were done, and data were kept only if the two agreed. We also performed a sensitivity analysis for the most important statistical parameters of our interaction score, ensuring that the main findings are robust to small parameter changes.

Randomization Duplicates of the same drugs were randomly distributed in the plates, instead of placed just next to each other, to avoid biases due to any plate spatial effect.

Blinding *in vitro* experiments/no blinding required

Reporting for specific materials, systems and methods

Materials & experimental systems

n/a	Involved in the study
<input checked="" type="checkbox"/>	<input type="checkbox"/> Unique biological materials
<input type="checkbox"/>	<input checked="" type="checkbox"/> Antibodies
<input checked="" type="checkbox"/>	<input type="checkbox"/> Eukaryotic cell lines
<input checked="" type="checkbox"/>	<input type="checkbox"/> Palaeontology
<input checked="" type="checkbox"/>	<input type="checkbox"/> Animals and other organisms
<input checked="" type="checkbox"/>	<input type="checkbox"/> Human research participants

Methods

n/a	Involved in the study
<input checked="" type="checkbox"/>	<input type="checkbox"/> ChIP-seq
<input checked="" type="checkbox"/>	<input type="checkbox"/> Flow cytometry
<input checked="" type="checkbox"/>	<input type="checkbox"/> MRI-based neuroimaging

Antibodies

Antibodies used

The anti-AcrA polyclonal primary antibody (custom made, Neovystems France) was provided by K.M. Pos (Goethe University, Frankfurt), and used in this study in 1:200,000 dilution in combination with an alkaline-phosphatase-conjugated anti-rabbit secondary antibody (A0545 Sigma, 1:5,000 dilution).

Validation

The anti-AcrA antibody was validated for specificity using the knockout strain.